

# DTIC FILE COPY



SECURITY CLASSIFICATION OF THIS PAGE

<b>REPORT DOCUMENTATION PAGE</b>		Form Approved OMB No. 0704-0188		
<b>AD-A217 378</b>		1b. RESTRICTIVE MARKINGS <p style="text-align: center;">NONE</p>		
3. DISTRIBUTION / AVAILABILITY OF REPORT APPROVED FOR PUBLIC RELEASE; DISTRIBUTION UNLIMITED.				
4. PERFORMING ORGANIZATION REPORT NUMBER(S)		5. MONITORING ORGANIZATION REPORT NUMBER(S) AFIT/CI/CIA-89-035		
6a. NAME OF PERFORMING ORGANIZATION AFIT STUDENT AT UNIV OF ARIZONA	6b. OFFICE SYMBOL (if applicable)	7a. NAME OF MONITORING ORGANIZATION AFIT/CIA		
6c. ADDRESS (City, State, and ZIP Code)		7b. ADDRESS (City, State, and ZIP Code) Wright-Patterson AFB OH 45433-6583		
8a. NAME OF FUNDING / SPONSORING ORGANIZATION	8b. OFFICE SYMBOL (if applicable)	9. PROCUREMENT INSTRUMENT IDENTIFICATION NUMBER		
8c. ADDRESS (City, State, and ZIP Code)		10. SOURCE OF FUNDING NUMBERS		
		PROGRAM ELEMENT NO.	PROJECT NO.	
		TASK NO.	WORK UNIT ACCESSION NO.	
11. TITLE (Include Security Classification) (UNCLASSIFIED) Structure and Dynamics of the Arizona Monsoon Boundary				
12. PERSONAL AUTHOR(S) Thomas Charles Adang				
13a. TYPE OF REPORT <del>MONO</del> /DISSERTATION	13b. TIME COVERED FROM _____ TO _____	14. DATE OF REPORT (Year, Month, Day) 1989	15. PAGE COUNT 121	
16. SUPPLEMENTARY NOTATION APPROVED FOR PUBLIC RELEASE IAW AFR 190-1 ERNEST A. HAYGOOD, 1st Lt, USAF Executive Officer, Civilian Institution Programs				
17. COSATI CODES		18. SUBJECT TERMS (Continue on reverse if necessary and identify by block number)		
FIELD	GROUP			SUB-GROUP
19. ABSTRACT (Continue on reverse if necessary and identify by block number)				
S DTIC ELECTE FEB 01 1990 D E				
90 02 01 013				
20. DISTRIBUTION / AVAILABILITY OF ABSTRACT <input checked="" type="checkbox"/> UNCLASSIFIED/UNLIMITED <input type="checkbox"/> SAME AS RPT. <input type="checkbox"/> DTIC USERS		21. ABSTRACT SECURITY CLASSIFICATION UNCLASSIFIED		
22a. NAME OF RESPONSIBLE INDIVIDUAL ERNEST A. HAYGOOD, 1st Lt, USAF		22b. TELEPHONE (Include Area Code) (513) 255-2259	22c. OFFICE SYMBOL AFIT/CI	

STRUCTURE AND DYNAMICS OF THE ARIZONA MONSOON  
BOUNDARY



by  
Thomas Charles Adang

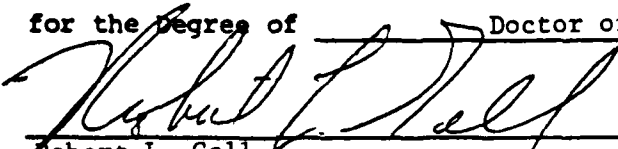
Accession For	
NTIS GRA&I	<input checked="" type="checkbox"/>
DTIC TAB	<input type="checkbox"/>
Unannounced	<input type="checkbox"/>
Justification	
By	
Distribution/	
Availability Codes	
Dist	Avail and/or Special
A-1	

A Dissertation Submitted to the Faculty of the  
DEPARTMENT OF ATMOSPHERIC SCIENCES  
In Partial Fulfillment of the Requirements  
For the Degree of  
DOCTOR OF PHILOSOPHY  
In the Graduate College  
THE UNIVERSITY OF ARIZONA

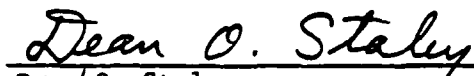
THE UNIVERSITY OF ARIZONA  
GRADUATE COLLEGE

As members of the Final Examination Committee, we certify that we have read  
the dissertation prepared by Thomas Charles Adang  
entitled Structure and Dynamics of the Arizona Monsoon Boundary

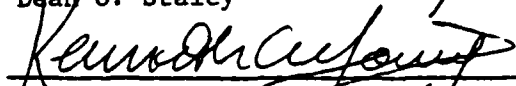
and recommend that it be accepted as fulfilling the dissertation requirement  
for the Degree of Doctor of Philosophy.

  
\_\_\_\_\_  
Robert L. Gall

3/31/89  
Date

  
\_\_\_\_\_  
Dean O. Staley

3/31/89  
Date

  
\_\_\_\_\_  
Kenneth C. Young

3/31/89  
Date

  
\_\_\_\_\_  
Benjamin M. Herman

3/31/89  
Date

  
\_\_\_\_\_  
Philip N. Slater

3/31/89  
Date

Final approval and acceptance of this dissertation is contingent upon the  
candidate's submission of the final copy of the dissertation to the Graduate  
College.

I hereby certify that I have read this dissertation prepared under my  
direction and recommend that it be accepted as fulfilling the dissertation  
requirement.

  
\_\_\_\_\_  
Dissertation Director

March 31, 1989  
Date

## STATEMENT BY AUTHOR

This dissertation has been submitted in partial fulfillment of requirements for an advanced degree at The University of Arizona and is deposited in the University Library to be made available to borrowers under rules of the Library.

Brief quotations from this dissertation are allowable without special permission, provided that accurate acknowledgement of source is made. Requests for permission for extended quotation from or reproduction of this manuscript in whole or in part may be granted by the head of the major department or the Dean of the Graduate College when in his or her judgement the proposed use of the material is in the interests of scholarship. In all other instances, however, permission must be obtained from the author.

SIGNED: Thomas C. Adair

## ACKNOWLEDGEMENTS

There are many people who have supported me as I strove to complete this dissertation, but several deserve special mention. First, I thank my dissertation director, Dr. Robert L. Gall, who first motivated my interest in the Arizona Monsoon and who was especially supportive during my last three years of writing in absentia. I also thank the other members of my advisory committee, Drs. Dean O. Staley, Kenneth C. Young, Benjamin M. Herman, and Philip N. Slater, for their advice and encouragement. The late Professor Louis J. Battan, an original member of my committee, was especially supportive during the formative stage of my research.

Second, I thank the Air Force Institute of Technology, which gave me the opportunity to pursue this course of study through its Civilian Institution program. Additionally, the understanding and encouragement of my Air Force supervisors, especially Lt. Cols. Robert E. Peterson and Robert G. Borchers, as I struggled to simultaneously complete the dissertation and accomplish my "normal" Air Force responsibilities are sincerely appreciated.

Most importantly, I am extremely thankful for the support of my family. The willingness of my wife and daughters, Jolyn, Jennifer, and Julie, to "share" me with work, travel, and completing the dissertation in absentia was crucial to its successful completion. I would not have finished without their support. Lastly, I acknowledge and thank my parents, Roberta J. Adang and the late William C. Adang, who instilled in me the importance of education and the life-long desire to pursue a graduate degree.

## TABLE OF CONTENTS

	Page
LIST OF ILLUSTRATIONS .....	6
LIST OF TABLES .....	10
LIST OF SYMBOLS .....	11
ABSTRACT .....	13
1. INTRODUCTION .....	16
2. NON-CONVENTIONAL DATA SOURCES .....	24
2.1 McIDAS products .....	25
2.1.1 VAS retrievals .....	25
2.1.2 VAS derived winds .....	28
2.1.3 Cloud track winds .....	32
2.1.4 VAS/cloud track wind assimilation .....	33
2.1.5 VAS gradient field analysis technique .....	34
2.2 FNOC cross sections .....	34
2.3 Lightning strike data .....	35
3. THE MONSOON BOUNDARY AT TUCSON, JUNE 1984 ..	37
3.1 Mean soundings .....	39
3.2 Time-height cross section .....	39
3.2.1 Temperature deviation from average .....	42
3.2.2 Mixing ratio .....	43
3.2.3 Wind velocity .....	43
3.2.4 Surface pressure .....	44
3.2.5 Summary .....	45
3.3 GOES imagery .....	46
4. TWO-DIMENSIONAL STRUCTURE OF THE MONSOON BOUNDARY .....	48
4.1 Composite cross section of the boundary	52
4.2 Secondary transverse circulation .....	57
4.3 Static stability .....	65
4.4 Tracer frontogenesis .....	67

## TABLE OF CONTENTS--Continued

	Page
4.5 Comparison with mid-latitude fronts ...	69
5. STRUCTURE OF THE MONSOON BOUNDARY FROM VAS DATA .....	75
6. WAVE DISTURBANCE ALONG THE MONSOON BOUNDARY .	86
6.1 Disturbance originating along the boundary .....	87
6.2 Disturbance interacting with the monsoon boundary .....	104
6.3 Conclusions .....	109
7. SUMMARY AND RECOMMENDATIONS FOR FUTURE RESEARCH .....	111
REFERENCES .....	119

## LIST OF ILLUSTRATIONS

Figure	Page
1.1 Mean streamline analysis for August (after Bryson and Hare, 1974) .....	19
1.2 Morning (0700 LST) dewpoint ( $^{\circ}$ F) at Tucson, AZ for 1977-1984. The series of dots below each dewpoint curve denote occurrence of precipitation at seven different stations spanning the Tucson valley. Each vertical position refers to a particular station .....	20
2.1 Graphical wind error analysis. R denotes radiosonde wind for station; V denotes closest VAS derived wind to that station; E is the error vector .....	30
3.1 Average morning and afternoon soundings at Tucson for one week prior to (18-23 June) and one week after (24-30 June) the onset of the 1984 summer monsoon. Light dashed lines are moist adiabats; light solid lines are dry adiabats. Heavy dashed lines are dewpoint curves; heavy solid lines are temperature curves .....	40
3.2 Time-height section at Tucson for 14 June - 10 July 1984: (a) Temperature deviation from average (June-Sept.) in $4^{\circ}$ C intervals; shaded areas are negative anomalies. (b) Mixing ratio in $4 \text{ g}\cdot\text{kg}^{-1}$ intervals; shaded areas exceed $8 \text{ g}\cdot\text{kg}^{-1}$ . (c) Wind velocity in standard notation. (d) Surface pressure with diurnal and semi-diurnal cycles removed .....	41
3.3 GOES $6.7 \mu\text{m}$ water vapor image at 1615Z 17 June 1984 .....	47
4.1 GOES $6.7 \mu\text{m}$ water vapor image at 2330Z 1 August 1985 .....	49

## LIST OF ILLUSTRATIONS--Continued

Figure	Page	
4.2	Upper figure shows cross section derived from FNOC analysis for 0000Z 2 August 1985. Solid contours are mixing ratio values in $\text{g}\cdot\text{kg}^{-1}$ ; wind velocities are in standard notation. Cross section runs from northwest of San Diego, CA to the western Gulf of Mexico. The lower figure shows the ageostrophic streamfunction ( $\text{m}\cdot\text{mb}\cdot\text{s}^{-1}$ ) computed for the same cross section .....	50
4.3	Features of the composite boundary: (a) Along-boundary winds ( $u$ ) in $\text{m}\cdot\text{s}^{-1}$ ; positive flow is into diagram. (b) Cross-boundary winds ( $v$ ) in $\text{m}\cdot\text{s}^{-1}$ ; positive flow is toward the left in the diagram; zero $v$ isotach denotes boundary location. (c) Temperature deviations from horizontal average in $^{\circ}\text{C}$ . (d) Ageostrophic circulation in $\text{m}\cdot\text{mb}\cdot\text{s}^{-1}$ . The line of the cross section is the same as Fig 4.2, although it spans a somewhat larger region because of the compositing. The western-most point in these sectors is toward the left .....	55
4.4	Upper figure shows the composite boundary ageostrophic streamfunction ( $\text{m}\cdot\text{mb}\cdot\text{s}^{-1}$ ) computed for geostrophic confluence (F2). Lower figure shows the composite boundary ageostrophic streamfunction ( $\text{m}\cdot\text{mb}\cdot\text{s}^{-1}$ ) computed for geostrophic horizontal shear (F1). Dashed lines are negative. Circulation is clockwise around positive maxima .....	63
4.5	Upper figure shows representative profiles of potential temperature ( $^{\circ}\text{K}$ ) on either side of the composite monsoon boundary. Lower figure shows representative profiles of equivalent potential temperature ( $^{\circ}\text{K}$ ) at same locations. Dashed lines indicate moist side of boundary; solid lines indicate dry side of boundary .....	66

## LIST OF ILLUSTRATIONS--Continued

Figure	Page
5.1 (a) GOES 6.7 $\mu\text{m}$ image at 0530Z 22 July 1985. (b) GOES 6.7 $\mu\text{m}$ image at 0530Z 23 July 1985. (c) GOES IR image at 0000Z 22 July 1985. (d) GOES IR image at 0000Z 23 July 1985 .....	76
5.2 Cloud-to-ground lightning-strike locations (dots) for 0000-0238Z, 23 July 1985. Dashed line denotes approximate location of monsoon boundary at that time, inferred from GOES 6.7 $\mu\text{m}$ imagery .....	78
5.3 Morning (0700 LST) dewpoint ( $^{\circ}\text{F}$ ) at Tucson for July 1985 .....	79
5.4 400 mb mixing ratio values ( $\text{g}\cdot\text{kg}^{-1}$ ) at 1648Z 22 July 1985, derived from VAS data. Solid line across southern Arizona and New Mexico is trace of cross section for Figure 5.5 .....	81
5.5 Cross sections of the deviations from the horizontal average for the trace depicted in Fig. 5.4 at 1648Z 22 July 1985. (a) Geopotential height (60m intervals). (b) Virtual temperature ( $^{\circ}\text{C}$ ). (c) Mixing ratio ( $\text{g}\cdot\text{kg}^{-1}$ ). Dashed lines denote negative values .....	82
6.1 A 36 hour sequence of GOES 6.7 $\mu\text{m}$ images (2315Z, 30 June - 1115Z, 2 July 1984) showing development of disturbance along monsoon boundary over southern Baja California .....	88
6.2 GOES 6.7 $\mu\text{m}$ image at 1115Z, 2 July 1984 .....	90
6.3 GOES visible image at 1415Z 2 July 1984 .....	92
6.4 Cloud-to-ground lightning strike data for 1800-1900Z, 2 July 1984 .....	93

## LIST OF ILLUSTRATIONS--Continued

Figure	Page
6.5 Smoothed maps of geopotential height (m) at 1418Z, 2 July 1984, derived from VAS data, for a) 400 mb and b) 700 mb. Cloud track wind (solid wind barbs) and RAOB wind (dashed wind barbs) data are also plotted. The heavy solid line denoted B-A is the trace of the cross section depicted in Figure 6.6 .....	96
6.6 Cross section of geopotential height deviation from horizontal average obtained from VAS data at 1418Z, 2 July 1984. Actual trace of cross section is shown in Figure 6.5. The dashed line indicates the trough axis .....	98
6.7 Cross sections of the deviations from the horizontal average of mixing ratio ( $\text{g}\cdot\text{kg}^{-1}$ ) and temperature ( $^{\circ}\text{K}$ ) along $28^{\circ}\text{N}$ from about $119^{\circ}$ - $109^{\circ}\text{W}$ at 1418Z 2 July 1984. Data derived from VAS retrievals .....	100
6.8 Six-hourly GOES IR images: 1200Z 30 July - 0600Z 31 July 1985 .....	106
6.9 Six-hourly GOES IR images: 1200Z 31 July - 0600Z 1 August 1985 .....	107
6.10 Six-hourly GOES IR images: 1200Z 1 August - 0600Z 2 August 1985 .....	108

## LIST OF TABLES

Table	Page
2.1 VAS retrieval/RAOB comparisons .....	29
3.1 Monsoon onset dates .....	38
4.1 Data input at composite boundary grid points .....	54
4.2 Maximum values of tracer frontogenesis components .....	70
4.3 Maximum values of velocity components .....	71
4.4 Maximum values for frontogenesis forcing ...	73
6.1 VAS retrieval/RAOB comparisons .....	95

## LIST OF SYMBOLS

$\alpha$	sequential overrelaxation coefficient
$c_p$	specific heat at constant pressure
$c_v$	specific heat at constant volume
C	Celsius temperature scale
f	Coriolis parameter
F	Fahrenheit temperature scale
F1	geostrophic shearing deformation
F2	geostrophic stretching deformation
g	magnitude of gravity
J	Jacobian operator, where
	$J_{yp}(\alpha, \beta) = \frac{\partial \alpha}{\partial y} \frac{\partial \beta}{\partial p} - \frac{\partial \alpha}{\partial p} \frac{\partial \beta}{\partial y}$
K	Kelvin temperature scale
m	along-boundary geostrophic absolute momentum
w	p-coordinate vertical motion
$\theta$	potential temperature
$\theta_e$	equivalent potential temperature
p	pressure
$p_0$	1000 mb pressure
$\psi$	streamfunction of the secondary circulation
q	mixing ratio
R	gas constant for dry air

## LIST OF SYMBOLS--Continued

$u$	total along-boundary velocity component
$U, u_a$	geostrophic and ageostrophic components of $u$
$V$	total horizontal velocity vector
$V_g, V_a$	geostrophic and ageostrophic vector components of $V$
$v$	total cross-boundary velocity component
$V, v_a$	geostrophic and ageostrophic components of $v$
$w$	z-coordinate vertical velocity

## ABSTRACT

The Arizona Monsoon Boundary is defined as the boundary separating two distinctly different air masses over Mexico, the southwestern United States, and the adjacent Pacific during the summer. The structure and dynamics of this boundary are examined by cross-sectional analysis using <sup>3</sup>three different data sources: 1) a time-height cross section, constructed using radiosonde observations, at the time the boundary initially passed through Tucson in 1984; 2) a composite cross section through the boundary, constructed from the Fleet Numerical Oceanography Center analysis; and 3) a cross section through the boundary using high-resolution fields of temperature, moisture, and geopotential height obtained from the VISSR Atmospheric Sounder (VAS). All three cross sections showed similar structure.

In some respects, the Arizona monsoon boundary resembles a mid-latitude front with a distinct and relatively sharp air mass change across the boundary, forced almost entirely by confluence. A direct ageostrophic circulation is produced by this forcing.

giving weak ascent on the warm, moist side of the boundary. The gradients and flow associated with the composite boundary are weaker, by a factor of <sup>4</sup>four, than those associated with strong mid-latitude fronts. However, the VAS cross section suggests that, at times, the strength of the boundary approaches that of middle-latitude fronts. The wind shear suggested by the composite boundary ought to be unstable to baroclinic or barotropic processes. Disturbances developing along the boundary have been observed.

One example of such a disturbance is examined using GOES imagery, lightning strike data, cloud track winds, and VAS data. Satellite images show the disturbance resembling a mid-latitude occluded cyclone, with an apparent low pressure center over northern Baja California and front-like cloud features extending eastward and southward from the low. Lightning strike data show convective activity occurring along the front-like features. Wind data indicate the presence of a cyclonic circulation south of San Diego along the Baja California coast. Cross sections using VAS data suggest that barotropic and baroclinic energy sources are present and suggest the front-like nature of the cloud feature extending

southward from the low pressure center. Additionally, a second disturbance that eventually interacted with the monsoon boundary is briefly examined using satellite imagery.

## CHAPTER 1

## INTRODUCTION

During the early summer season, the southwestern United States and northern Mexico are under the influence of a hot, dry, continental tropical (cT) air mass (Peterssen, 1956; Battan, 1984). However, between latter June to early July, this region experiences a change in air mass from cT to maritime tropical (mT) and normally remains under its influence through September. A dramatic increase in precipitation occurs at Tucson due to the change in air mass; Tucson averages 5.91 inches of rain from 1 July through 30 September, while averaging only 5.18 inches during the remainder of the year. This change in the rainfall is typical of many Southwest stations; over Arizona, more than 40 percent of annual rainfall occurs during this same 3 month period (Jurwitz, 1953).

The change in air mass is due to a northward shift of the axis of the surface subtropical ridge so that it lies north of the region (Bryson and Lowry, 1955). In general, as the ridge shifts to the north,

the prevailing winds change from westerly to southeasterly across the southwestern United States. This seasonal reversal of the wind flow satisfies the standard definition of a monsoon circulation (Huschke, 1959) and, for over 30 years, this shift to southeasterly flow has been termed the Arizona Monsoon.

The Arizona Monsoon is obviously important to those people residing in the southwestern U.S. and northern Mexico. However, in the rest of the country, the concept of a monsoon in the southwestern United States is not well known, even among the meteorological community. Research to date is descriptive in nature and emphasizes the synoptic scale monsoon circulation and sources of moisture associated with the monsoon (Bryson and Lowry, 1955; Bryson, 1957; Reitan, 1957; Brenner, 1973; Hales, 1974).

Bryson and Lowry (1955), Bryson and Hare (1974), and Tang and Reiter (1984) describe the monsoon circulation in some detail. At the surface during the summer, the western United States and eastern Pacific are dominated by a subtropical ridge. High pressure centers are located over the eastern Pacific and western Atlantic oceans, and the highs are split by the continent. Over the eastern Pacific, the flow is

generally northwesterly, while the flow over Mexico is generally southeasterly. The air mass over Mexico is generally moist and the air mass over the adjacent Pacific is generally dry above the boundary layer. Thus, there must be a boundary separating them.

Figure 1.1 shows mean surface streamlines for August from Bryson and Hare (1974) and illustrates the circulation about the subtropical highs and the boundary that must exist between them. The data presented herein suggest this boundary is further west (off the Mexican coast) than indicated by Bryson and Hare; however, the concept of a convergence zone is clearly indicated. This boundary separating the two air masses is termed the Arizona monsoon boundary. In this work, the structure and dynamics of the boundary will be discussed and its similarities with mid-latitude fronts will be demonstrated.

Figure 1.2 gives a graphical description of the impact of both the monsoon and the passage of the monsoon boundary on Tucson's weather. The series of dots below each dewpoint curve denote the occurrence of precipitation at seven different stations spanning the Tucson valley. If all seven are present on a given day, then precipitation, nearly all of which

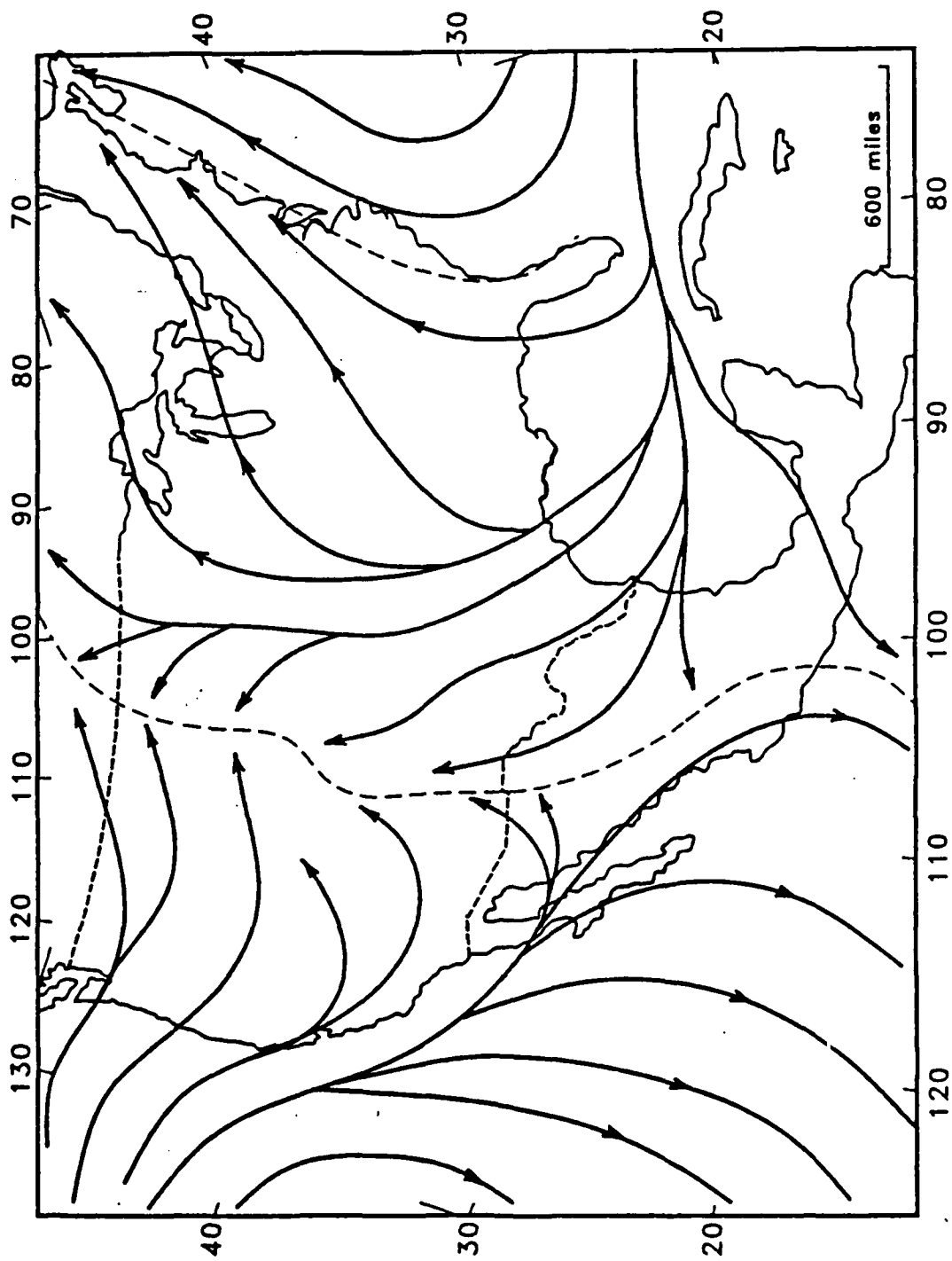


Figure 1.1. Mean streamline analysis for August (after Bryson and Hare, 1974).

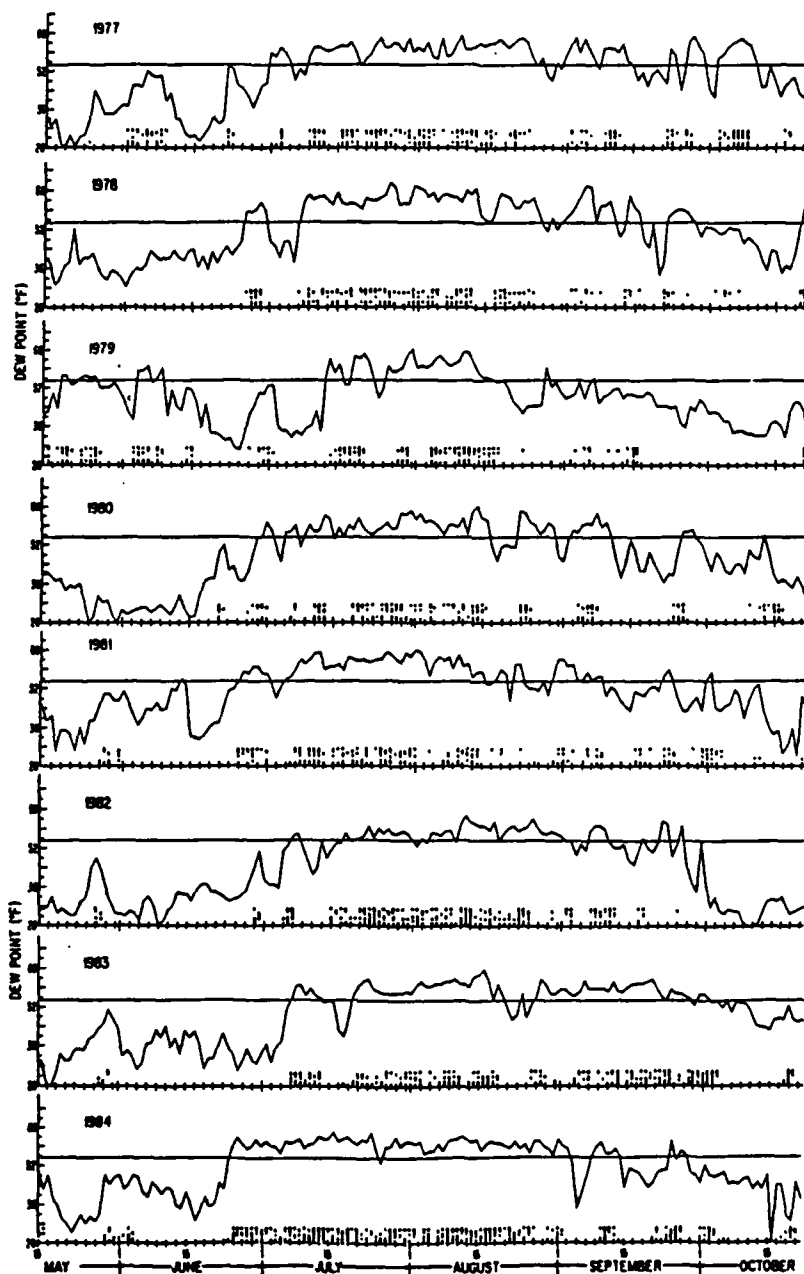


Figure 1.2. Morning (0700 LST) dewpoint ( $^{\circ}$ F) at Tucson, AZ for 1977-1984. The series of dots below each dewpoint curve denote occurrence of precipitation at seven different stations spanning the Tucson valley. Each vertical position refers to a particular station.

results from thunderstorms, is fairly widespread. Note that there are often rapid transitions from dry conditions in June to a rather uniformly wet air mass, in which precipitation is frequent, in July through September.

Some years, the transition occurs in stages, while in others (e.g., 1983 and 1984) the transition occurs within a day or two. This transition to wet conditions represents the passage of the monsoon boundary and, as shown later, the transition between westerly and southeasterly winds above 750 mb. Periods of drying after the initial transition to a wet air mass are also evident in Figure 1.2 (see 19 July 1983). This drying is common and results from the brief return of westerlies to Tucson, normally due to the passage of strong short waves through the northern United States. The return of the moisture is usually just as abrupt as the initial onset, suggesting that this boundary between moist and dry air remains quite sharp. A good example of this was on 19 July 1983.

The structure of the monsoon boundary is not well understood owing principally to a scarcity of conventional data over the southwestern United States,

northern Mexico, and the eastern Pacific. Although sufficient for describing the synoptic scale monsoon circulation, the radiosonde network is, by itself, spatially too coarse to adequately describe its horizontal structure. However, using high resolution fields of temperature, moisture, and wind derived from satellite data (imagery and soundings), assimilated with conventional data, a relatively complete description of the structure and dynamics of the monsoon boundary can be provided.

The purpose of this work, then, is two-fold: (a) to describe the structure and dynamics of the Arizona monsoon boundary and demonstrate its similarities with mid-latitude fronts, using conventional and high resolution satellite-derived data; and (b) to show that disturbances along the boundary exist.

Chapter 2 discusses the non-conventional data used to describe the structure and dynamics of the monsoon boundary in subsequent chapters.

Chapter 3 describes the structure of the Arizona monsoon boundary at Tucson in June 1984 through cross-sectional analysis using Tucson radiosonde observations (RAOBS) and satellite imagery.

Chapter 4 describes the two-dimensional structure of the monsoon boundary using a composite cross section derived from a set of August 1985 cross sections obtained from the Fleet Numerical Oceanography Center (FNOC).

Chapter 5 discusses the structure of the monsoon boundary determined through the use of high-resolution temperature, moisture, and geopotential height data obtained from the Visible and Infrared Spin Scan Radiometer (VISSR) Atmospheric Sounder (VAS) on the Geostationary Operational Environmental Satellite (GOES). That structure is then compared to those determined in Chapters 3 and 4.

Chapter 6 presents two examples of disturbances associated with the monsoon boundary: (a) a wave disturbance that appears to originate along the monsoon boundary, which may be unstable with respect to barotropic and baroclinic disturbances; and (b) an apparent easterly wave that interacted with the monsoon boundary.

Chapter 7 summarizes the major findings and provides recommendations for future study.

## CHAPTER 2

## NON-CONVENTIONAL DATA SOURCES

Due to the sparsity of data in the region of the monsoon boundary, one must use "non-conventional" data sources to better describe the two dimensional structure of the boundary. "Non-conventional" means data other than that derived from the surface or rawinsonde network.

The non-conventional data came from four sources: Man/computer Interactive Data Access System (McIDAS), FNOC, Bureau of Land Management (BLM) lightning detection network, and Detachment 13, 25th Weather Squadron, Davis-Monthan Air Force Base, Arizona. McIDAS provided high resolution fields of temperature, moisture, and geopotential height using the VAS data, as well as imagery from GOES. FNOC provided a set of 0000Z cross-sections through the monsoon boundary for eleven days in August 1985. The BLM network provided cloud-to-ground lightning-strike data for Arizona, New Mexico, and parts of northern Mexico during the summers of 1984 and 1985. Det 13, 25WS provided GOES data (visible, infrared, and 6.7  $\mu\text{m}$  imagery) as well

and augmented our conventional data set with RAOBS for Tucson and selected Mexican stations.

## 2.1 McIDAS products

McIDAS, an interactive video display computer system at the University of Wisconsin's Space Science and Engineering Center, permits rapid access to and display of various types of meteorological data. McIDAS not only provides real-time access to GOES imagery, but also provides access to archived satellite imagery, satellite soundings, surface reports, and RAOBS. Suomi et. al. (1983) and Wash and Whittaker (1980) give a more complete description of McIDAS capabilities and applications.

### 2.1.1 VAS retrievals

The VAS dwell sounding (DS) mode produces the radiance measurements necessary to construct profiles of temperature and moisture in a cloud-free environment. Spatially, VAS temperature and moisture soundings are available at a horizontal resolution of 20-75 km (Jedlovec, 1985). VAS retrievals are possible every 30 minutes, although normally available every 1-3 hours.

The obvious strength of the satellite sounding process is the substantially increased temporal and spatial coverage of the atmosphere compared to conventional observing networks. However, there are several weaknesses that limit the utility of VAS soundings: poor vertical resolution, cloud contamination, and lack of consistent availability. The broad weighting functions of the VAS channels give poor vertical resolution; Jedlovec (1985) places that resolution at approximately 200 mb. Clouds contaminate the soundings, so soundings must occur in a cloud-free environment.

During the summer season, higher priority needs of the National Severe Storms Forecast Center limited VAS availability to roughly 1000Z to 1800Z on convectively active days (Birkenheuer and Snook, 1985). Also, with the failure of GOES-5 in July 1984, GOES-6 was the only VAS satellite available for forecasting support and research activity until the launch of GOES-7 in February 1987. Despite these weaknesses and the errors described below, VAS data are extremely useful in depicting mesoscale horizontal structure of the atmosphere.

The most useful and detailed analysis of errors inherent in VAS soundings are based on data obtained from the 1982 AVE/VAS Ground Truth Field Experiment. During the experiment, three-hourly rawinsonde measurements were made over a regional mesoscale network concurrently with VAS DS mode measurements (Hill and Turner, 1983). Jedlovec (1985) and Fuelberg and Meyer (1986) evaluated the accuracy and representativeness of VAS data from different retrieval algorithms using the satellite and rawinsonde data from this experiment.

Jedlovec (1985) concluded that gradients of basic and derived (precipitable water and thickness) parameters show good horizontal structure and resemblance to actual gradients. Thus, gradient information can be used to infer mesoscale structure. In fact, Jedlovec (1985) and Hayden and Schreiner (1984) strongly recommend that gradient patterns derived by satellite retrievals be used. Fuelberg and Meyer (1986) reported that the mesoscale gradient information from VAS shows a slight reduction in magnitude compared to gradient information obtained from the Ground Truth Field Experiment. This reduction is probably due to the sampling difference

between the two methods; VAS provides a volumetric sampling of the atmosphere while radiosondes provide point measurements.

#### 2.1.2 VAS derived winds

Geostrophically derived winds from VAS retrievals contain errors that rendered them unusable for this work. Table 2.1 shows a comparison of VAS derived data on 22 July 1984 (the data that will be described in Chapter 5) with the Tucson RAOBS. Note that the wind direction differences at some levels approach 180°. Similar errors were found when different VAS data were compared with RAOBS from other stations. On the other hand, temperature and humidity values compare well (temperature better than humidity, although there are differences).

Figure 2.1 is a graphical wind error analysis of the data for 1418Z 2 July 1984 that will be described in Chapter 6. The figure compares radiosonde measured winds for three stations (Tucson, San Diego, and Guaymas) to geostrophically derived winds from the VAS retrievals closest to the stations. The retrievals are within 60 km of the stations; the radiosonde data preceeds the VAS data by over 2 hours. The error vectors for each comparison are significant and fairly

TABLE 2.1. VAS Retrieval/RAOB Comparisons

VAS Data, 1648Z 22 July 1985				
P(mb)	T(°C)	W(g·kg <sup>-1</sup> )	Z(m)	Wind Dir/Speed (deg/m·s <sup>-1</sup> )
Surface	27	13.1		
850	22	9.4	1516	120/02
700	9	1.8	3160	140/03
500	-8	2.9	5862	160/06
400	-17	0.2	7567	170/07
300	-32	-	9660	190/06
200	-53	-	12321	200/06
Tucson RAOB, 1200Z 22 July 1985				
P(mb)	T(°C)	W(g·kg <sup>-1</sup> )	Z(m)	Wind Dir/Speed (deg/m·s <sup>-1</sup> )
Surface	24	14.1		170/03
850	22	11.0	1510	250/02
700	10	8.5	3170	340/04
500	-7	3.7	5870	030/01
400	-16	0.2	7580	310/02
300	-32	-	9690	300/04
200	-54	-	12410	330/09

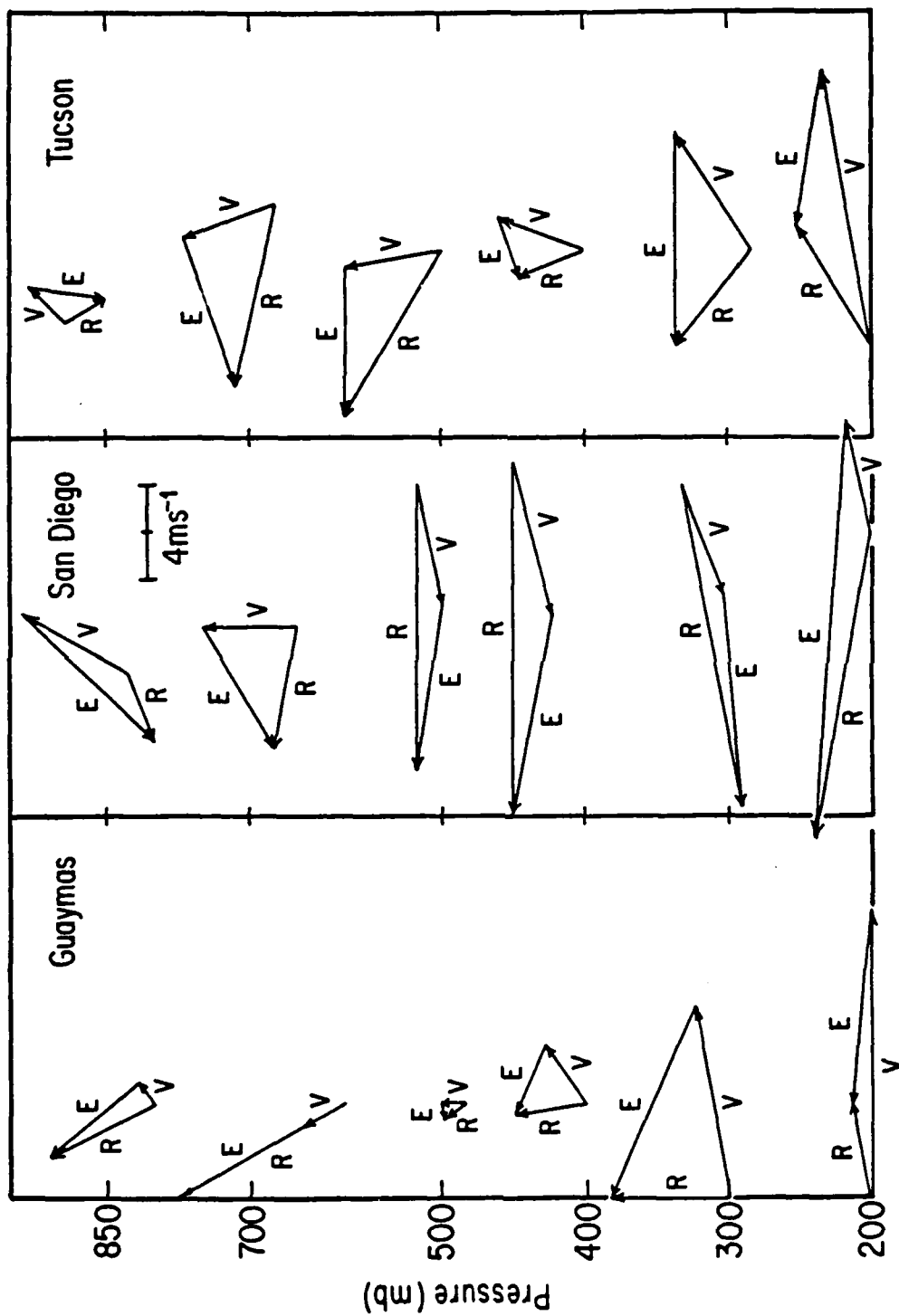


Figure 2.1. Graphical wind error analysis. R denotes radio-sonde wind for station; V denotes closest VAS derived wind to that station; E is the error vector.

constant, both in height and between comparisons. For the most part, the error vectors are easterly in direction. The mean speed errors and standard deviations for the three stations in Figure 2.1 range from 5.2-9.3  $\text{m}\cdot\text{s}^{-1}$  and 2.4-4.4  $\text{m}\cdot\text{s}^{-1}$ , respectively.

There are probably two main sources for the errors in VAS derived winds. First, as Jedlovec (1985) points out, some VAS mesoscale gradients do not parallel those of the radiosonde network. An error in the orientation of the geopotential height gradient leads, of course, directly to errors in the geostrophically derived winds. The error in orientation could be due to an error in the first guess field. The result of the VAS retrieval scheme, achieved by perturbing the first guess, is not independent of the first guess; in fact, the better the first guess, the better the retrieval. Second, with differences in surface elevation, errors may be introduced at the surface and propagate upward through the retrieval. Whatever the cause, the error in VAS geostrophically derived winds appear substantial enough to preclude their use in this study.

### 2.1.3 Cloud track winds

Mosher (1978) and Menzel et. al. (1983) describe methods to obtain winds from cloud motions on GOES images. One loads three consecutive half-hourly visible images in McIDAS and follows the changes in location of identifiable cloud elements in time, either by a direct operator controlled tracking or by a cross-correlation method that matches small patterns in the successive images. The three images yield two estimates of the wind which are compared and rejected if they differ by a set threshold.

Wilson and Houghton (1979) estimate the standard error of the difference in cloud drift wind and RAOB wind reports at  $4.7 \text{ m}\cdot\text{s}^{-1}$ . One substantial weakness of cloud drift winds is the lack of uniform coverage at any one altitude. When a fairly uniform cloud layer is present (i.e., stratiform deck), individual cloud elements are hard to distinguish. Cloud track winds are also prone to directional errors if cloud elements are not tracked carefully among the three images. This error can be minimized by comparing the two wind estimates and rejecting the estimates if the wind direction differs by more than a set threshold. Lastly, the clouds may not move with the wind (i.e.,

clouds "stuck" to a mountain). Cloud track winds are used in the Chapter 6 case study.

Stewart et. al. (1985) describe how to produce water vapor drift winds using hourly water vapor imagery. Water vapor drift winds give uniform horizontal coverage of mid-level wind flow (normally about 400 mb) at the synoptic scale. The "trackability" of water vapor inhomogeneities is much more difficult than cloud elements; many of these features are indistinguishable through the required sequence of images. The vector difference between water vapor winds and conventionally measured winds is about  $8 \text{ m}\cdot\text{s}^{-1}$ . Since the vector difference for water vapor winds is almost as large as the wind maximum in the monsoon circulation, these winds are not used in this study.

#### 2.1.4 VAS/cloud track wind assimilation

Simultaneously using VAS retrieval and cloud track winds to examine the structure of the boundary poses a problem. Cloud track winds are only available where clouds are present and VAS inversions are only available where there are no clouds. However, a good mix is normally possible during summer mornings (1000-1800Z) before cloud cover builds extensively. Using

morning cases also increases the probability of VAS retrieval availability, as mentioned previously.

#### 2.1.5 VAS gradient field analysis technique

For each VAS retrieval area, McIDAS allows one to generate fields of certain meteorological parameters at mandatory pressure levels. For this study, fields of temperature, mixing ratio, and geopotential height at the mandatory pressure levels from the surface to 200 mb (400 mb for mixing ratio) were used. To use the strength of the retrievals (horizontal gradient fields), cross sections were constructed through the retrieval area, parameters averaged at each pressure level, and the deviations from average calculated at those levels.

#### 2.2 FNOC cross sections

FNOC provided a set of 0000Z cross sections for eleven days in August 1985. These were taken from their global analyses, which include satellite and conventional data. Furthermore, forecasts are used as a first guess in data sparse regions. The first guess will at least contain fields that result from the large scale forcing present in the model. Thus, the synoptic scale subtropical highs are depicted quite

well. Small scale disturbances, on the otherhand, may be poorly resolved in the data poor areas.

The monsoon boundary, which is just the boundary between the subtropical highs, may be sufficiently resolved to obtain at least a mean depiction of its structure. These cross sections provide the basis for examining the monsoon dynamics in Chapter 4. They represent as good a data set as is currently possible in this area.

### 2.3 Lightning-strike data

The BLM provided available cloud-to-ground lightning-strike data for the summers of 1984 and 1985. The data can be displayed on user-defined maps and is available for the western United States. Reap (1986) points out the importance of lightning strike data in locating convective activity not seen by radar in the mountainous terrain of the desert Southwest. For the summers of 1983 and 1984, 41 percent of the over 2 million lightning strikes occurred when no radar echoes were reported and 87 percent of the strikes occurred with radar intensity levels below the threshold normally used for delineating thunderstorms in the eastern United States. These data are used in

conjunction with satellite imagery to help locate thunderstorms.

Krider et. al. (1980) give error and efficiency estimates for the cloud-to-ground lightning strikes detected by the BLM network. Less than 2 percent of cloud-to-ground flashes are falsely accepted and 98 percent of atmospheric noise is rejected. No direct measurements of detection efficiency are available for the BLM network. However, individual direction finders have efficiency estimates of 80-90 percent for ranges less than 400 km for Arizona locations. Reap (1980) estimates the BLM network efficiency to be 50-70 percent and states that the estimate is probably conservative.

## CHAPTER 3

## THE MONSOON BOUNDARY AT TUCSON, JUNE 1984

The Phoenix Weather Service Office (WSO) defines the onset of the Arizona Monsoon for Phoenix as the first day of three consecutive days during which the daily average surface dewpoint temperature equals or exceeds 55°F. Table 3.1 displays the monsoon onset dates at Tucson for 1966-1985 using the Phoenix WSO definition. Another coarse definition of monsoon onset, suggested by Figure 1.2, is the beginning of nearly continuous high surface dewpoint with coincident periods of precipitation. Using the latter definition, the onset dates for 1983 and 1984 were 7 July and 25 June, respectively. Those dates exactly match the Phoenix WSO onset dates for 1983 and 1984 listed in Table 3.1. The onset dates listed in Table 3.1 are often a day late when the boundary passes through Tucson late in the day, since those dates rely on a daily average dewpoint.

TABLE 3.1. Monsoon Onset Dates

Year	Date
1966	June 28
1967	June 18
1968	July 4
1969	July 8
1970	July 18
1971	July 3
1972	July 13
1973	July 4
1974	July 1
1975	July 2
1976	June 29
1977	July 2
1978	July 8
1979	July 16
1980	July 12
1981	June 27
1982	July 6
1983	July 7
1984	June 25
1985	July 14

### 3.1 Mean soundings

To characterize the air mass change that occurs with the passage of the boundary, one week of Tucson RAOBS were averaged both prior to and after the transition to moist conditions at Tucson on 24 June 1984 (this will also be called the onset of the monsoon in 1984). Morning and afternoon soundings were averaged separately to remove the strong diurnal variation in temperatures in the lower troposphere that is characteristic of the desert Southwest.

Figure 3.1 shows the two average soundings. Two features are immediately obvious. First, there is a distinct air mass change, evidenced by a substantial increase in vertical moisture distribution after the onset for both morning and afternoon soundings. Second, there is a change in the vertical temperature distribution. Both soundings show a change to a more moist adiabatic lapse rate.

### 3.2 Time-height cross section

A time-height cross section of four parameters was constructed for Tucson for the period 15 May - 22 October 1984. Figure 3.2 displays a portion of the cross-section through the time of the monsoon onset. Each panel from Figure 3.2 is described below.

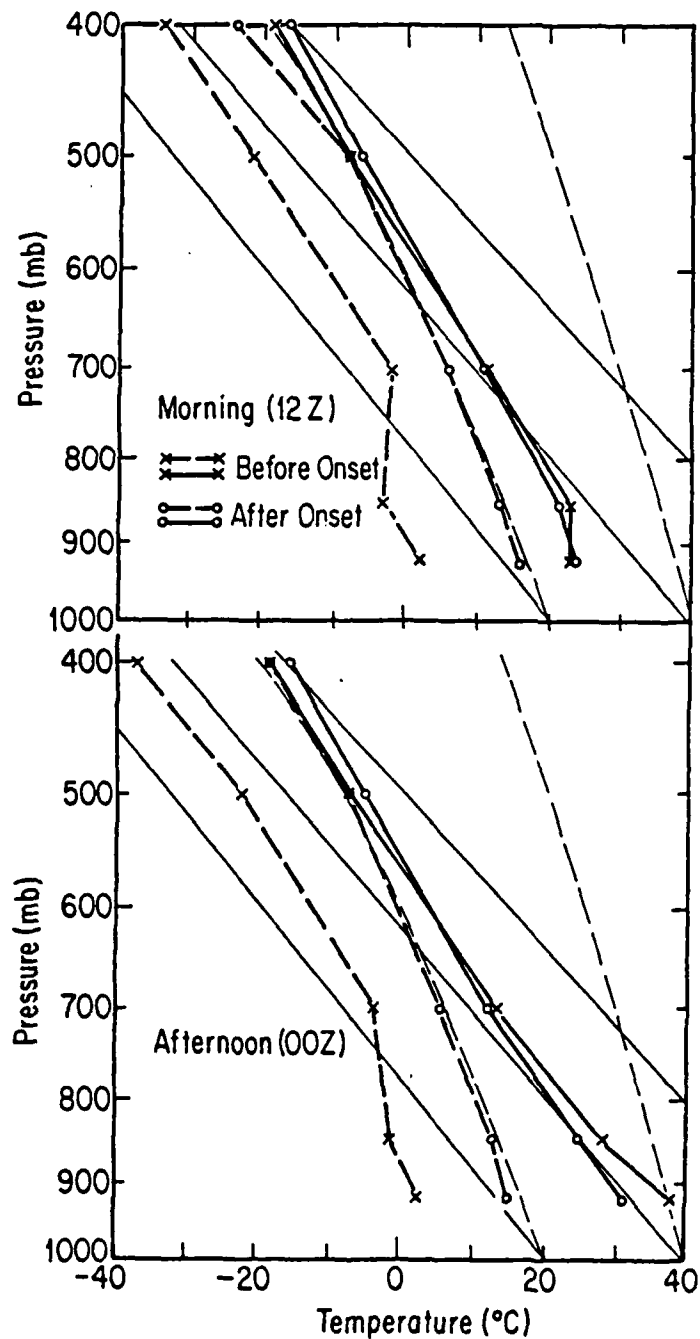
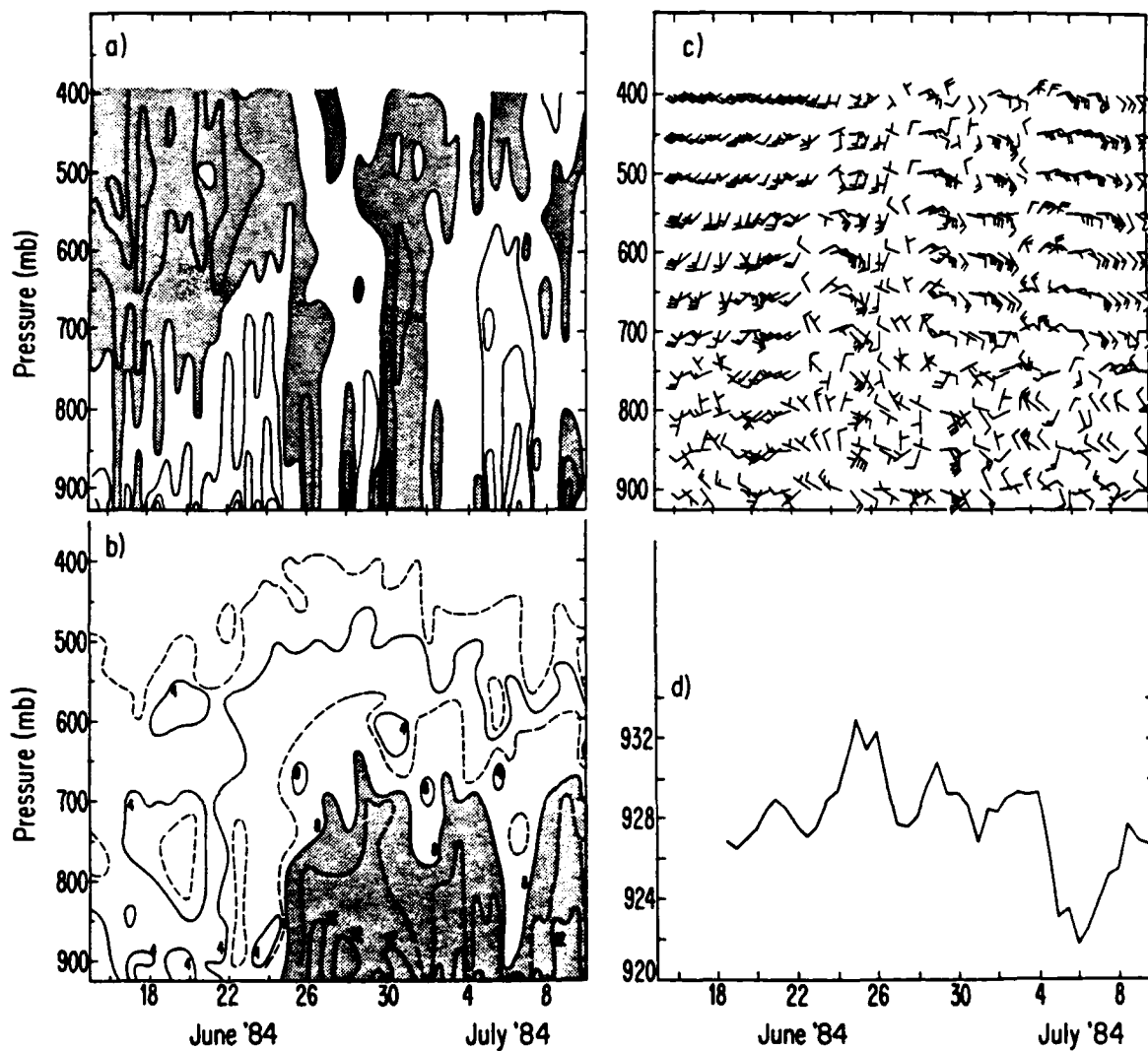


Figure 3.1. Average morning and afternoon soundings at Tucson for one week prior to (18-23 June) and one week after (24-30 June) the onset of the 1984 summer monsoon. Light dashed lines are moist adiabats; light solid lines are dry adiabats. Heavy dashed lines are dewpoint curves; heavy solid lines are temperature curves.



**Figure 3.2** Time-height section at Tucson for 14 June - 10 July 1984: (a) Temperature deviation from average (June-Sept.) in  $4^{\circ}\text{C}$  intervals; shaded areas are negative anomalies. (b) Mixing ratio in  $4 \text{ g}\cdot\text{kg}^{-1}$  intervals; shaded areas exceed  $8 \text{ g}\cdot\text{kg}^{-1}$  (c) Wind velocity in standard notation. (d) Surface pressure with diurnal and semi-diurnal cycles removed.

### 3.2.1 Temperature deviation from average

Daily absolute temperature changes during the summer are relatively small. Therefore, to more readily depict temperature changes resulting from the passage of the boundary, temperature deviations from a time average at the various levels were calculated. Morning and afternoon soundings were averaged and the deviations calculated separately to eliminate the strong diurnal variations in lower levels. The maximum deviation above the surface layer is  $8^{\circ}\text{C}$ ; for the most part, though, deviations are  $4^{\circ}\text{C}$  or less.

The temperature deviations clearly show the air mass change taking place at monsoon onset (on 24 June). The more unstable lapse rates dominant prior to onset clearly stand out in Figure 3.2a, with warmer lower tropospheric temperatures and cooler upper tropospheric temperatures. After monsoon onset, the temperature anomalies are more uniform throughout the depth of the troposphere, as compared to the period before the onset.

This illustrates the difference in lapse rates between the air masses on either side of the boundary. The alternating warm and cold anomalies that occur

after the onset may represent the passage of disturbances that are part of the monsoon circulation. Further discussion of some of these disturbances (beyond those described in Chapter 6) will be provided in future work.

### 3.2.2 Mixing ratio

Figure 3.2b shows the time-height cross section of mixing ratio for the same period as Figure 3.2a. The units are  $\text{g}\cdot\text{kg}^{-1}$  and the shaded area denotes mixing ratio values greater than  $8 \text{ g}\cdot\text{kg}^{-1}$ . Prior to onset, the atmosphere is well mixed, with mixing ratios near the surface generally below  $4 \text{ g}\cdot\text{kg}^{-1}$ . On 24 June there is a rapid transition to much more humid conditions, with surface mixing ratios rising above  $10 \text{ g}\cdot\text{kg}^{-1}$  in less than twelve hours and mixing ratios above  $8 \text{ g}\cdot\text{kg}^{-1}$  extending above 700 mb. After the onset of the monsoon on 24 June, mixing ratios above  $12 \text{ g}\cdot\text{kg}^{-1}$  near the surface were common and high values of mixing ratio extended above 700 mb.

### 3.2.3 Wind velocity

Figure 3.2c shows the time-height cross section of wind velocity. Prior to onset of the monsoon, the winds were generally out of the southwest above 750

mb. On 24 June, the day the moisture increased abruptly, winds switched from northwest or westerly to south or southeasterly within the interval between the soundings. After 23 June, winds above 700 mb were generally from the east or southeast. The deep layer of southeasterly flow is typical of the flow during the summer monsoon period in Tucson. Note that, after the onset, there were several periods where winds with light westerly components are evident. These periods represent the passages of weak disturbances associated with the monsoon circulation that were noted earlier.

#### 3.2.4 Surface pressure

Figure 3.2d shows the surface pressure during the same times as the cross sections. Here, the diurnal variation has been removed by computing the diurnal and semi-diurnal Fourier components from June through August 1984 and then subtracting the resulting series from the full time series of pressure.

Note that there is a distinct minimum in the pressure about one day before the passage of the boundary on 24 June. Thus, the boundary appears to lie more or less in a trough of low pressure, although the trough clearly precedes the distinct moisture change. This same relation between the pressure and

the moisture gradient is evident in the case study discussed in Chapter 5. The troughs and ridges that passed through Tucson after the 24th are associated with the disturbances noted earlier.

### 3.2.5 Summary

From Figure 3.2, it is evident that the passage of the monsoon boundary over a particular station, such as Tucson, results in a transition to an air mass that is significantly warmer above 700 mb and much moister through all levels in the lower troposphere. Furthermore, cooler conditions near the surface and warmer aloft imply that the moist air mass is closer to moist adiabatic (Figure 3.1) than the dry air mass preceding the passage of the boundary. Due to the increase in low level moisture, this suggests an air mass in which moist convection is more prevalent (see Figure 1.2).

As the boundary passes, there is a dramatic change in wind direction from southwest to southeast. The transition between the air masses is quite sharp, with most of the gradients passing between the radiosonde ascents, or in about 12 hours. In some respects, the passage of the monsoon boundary through Tucson in 1984 was like the passage of a front in

middle latitudes, i.e., there was a distinct and relatively sharp air mass change.

### 3.3 GOES imagery

Figure 3.3 illustrates what the monsoon boundary looks like in the 6.7  $\mu\text{m}$  GOES imagery. This figure is from 17 June 1984 or about one week prior to the passage of the boundary through Tucson. Light areas on these images represent relatively moist conditions in the middle troposphere (400 mb) while dark regions represent drier conditions. The whitest regions are clouds.

On 17 June, there was a distinct line in western New Mexico separating a light, moist region over New Mexico from a dark, dry region over Arizona. Note from Figure 3.2 that Tucson, at this time, was dry at all levels. Such a line is seen frequently in the 6.7  $\mu\text{m}$  imagery in the summer, which suggests that it is a good representation of the location of the monsoon boundary. More discussion of these images and their relevance to the monsoon boundary will be presented in later sections.

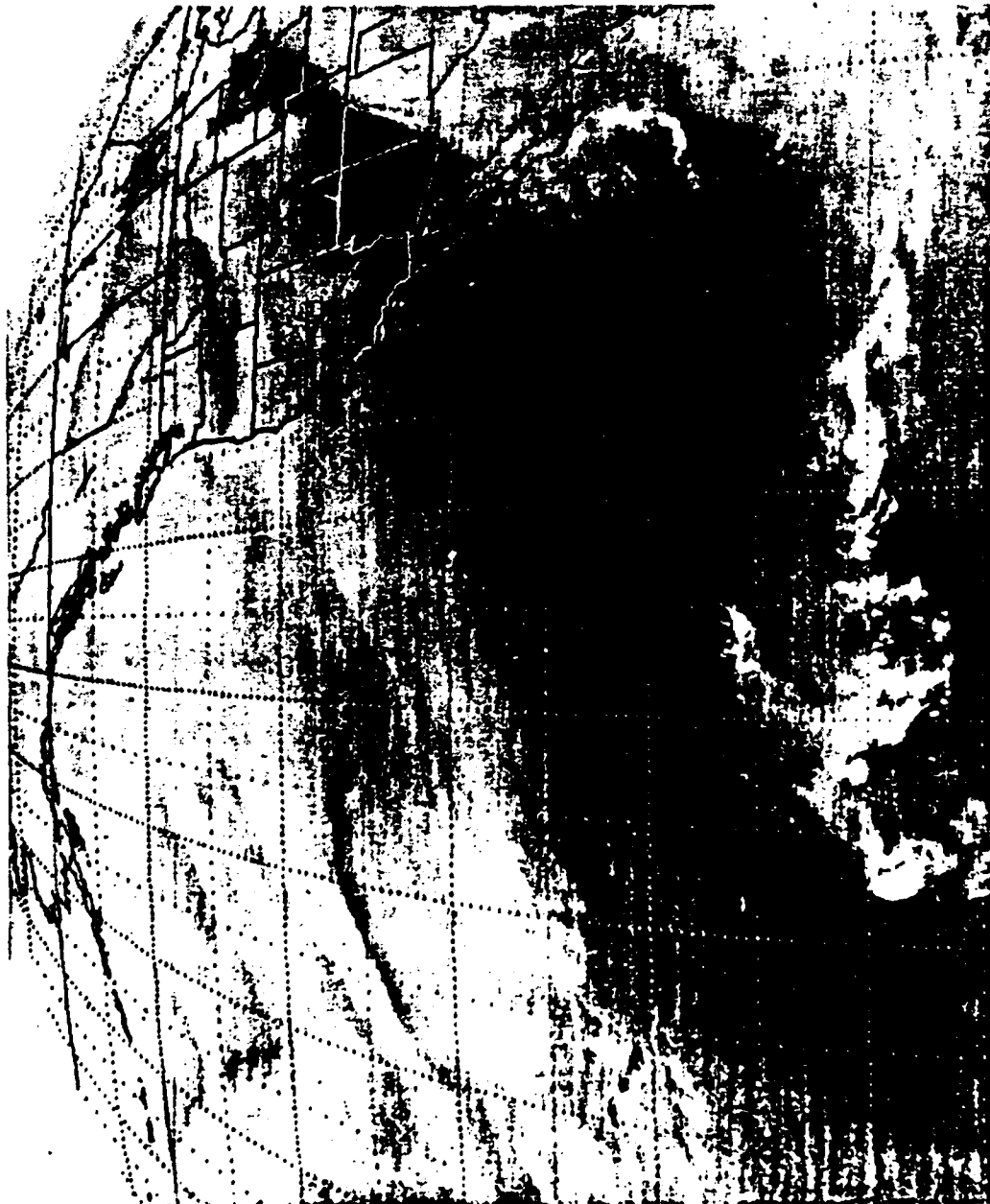


Figure 3.3 GOES 6.7  $\mu\text{m}$  water vapor image at 1615Z 17 June 1984.

## CHAPTER 4

## TWO-DIMENSIONAL STRUCTURE OF THE MONSOON BOUNDARY

During August 1985, the monsoon boundary was readily evident in a sequence of 6.7  $\mu\text{m}$  images as a nearly straight, abrupt boundary separating dry and moist air masses. Figure 4.1 is a 6.7  $\mu\text{m}$  image of the boundary at 2330Z 1 August 1985, which is oriented from north-northeast to south-southwest through central Arizona and northwestern Mexico. Throughout August 1985, the boundary generally maintained this orientation, although it did oscillate longitudinally. The boundary was examined using 0000Z FNOC cross sections for eleven days in August 1985. All cross sections are more or less perpendicular to the boundary and run from west-northwest of San Diego CA, across northern Mexico, to the western Gulf of Mexico (see Figure 4.2 for coordinates).

Figure 4.2 shows one such cross-section for 2 August 1985; the location of the boundary is roughly at center and delineated by winds with a westerly component to the west and an easterly component to the

2330 01AU85 38E-4ZA 00582 10581 UC5

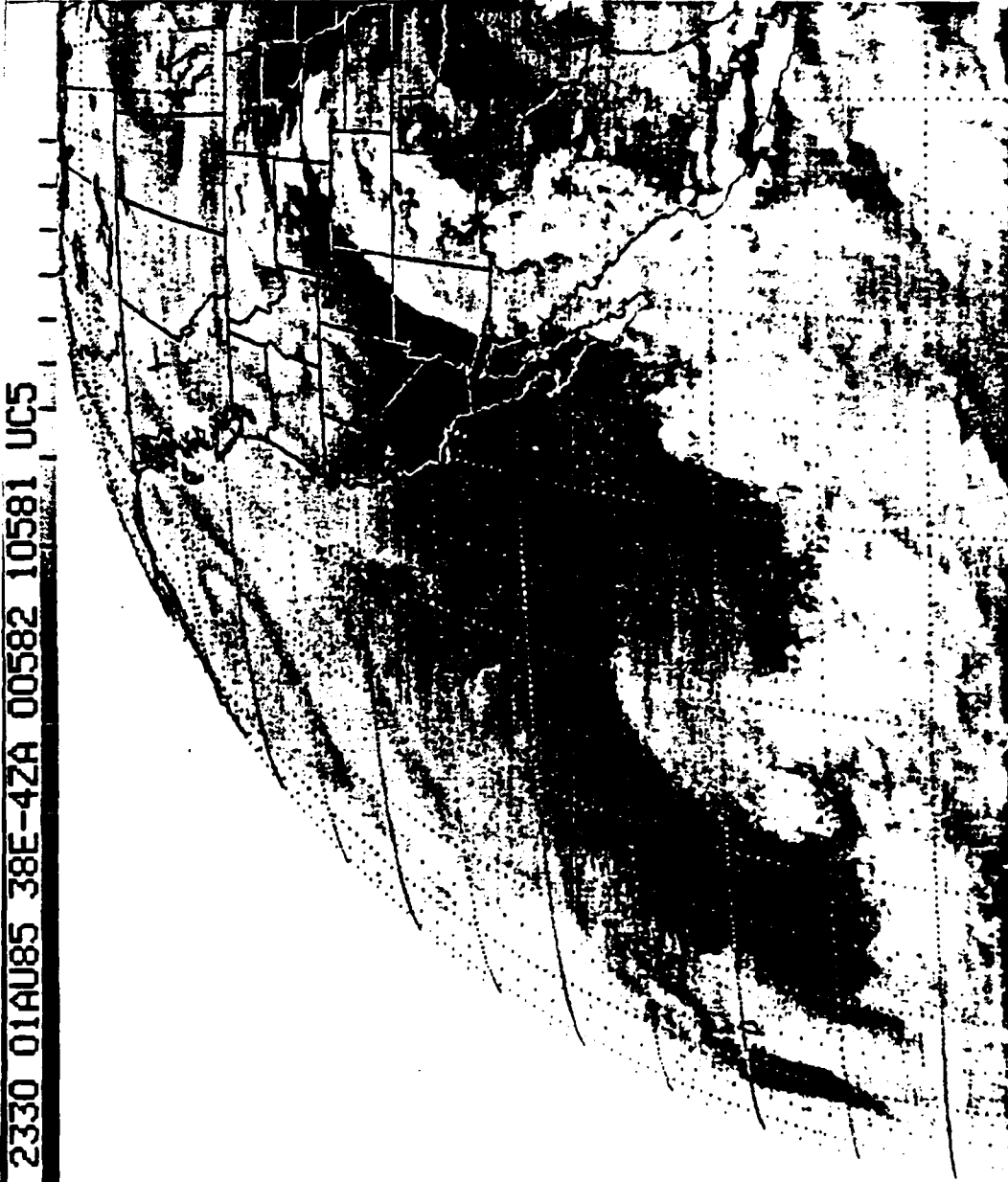


Figure 4.1 GOES 6.7  $\mu\text{m}$  water vapor image at 2330Z 1 August 1985.

2 August, 1985 - 00Z

50

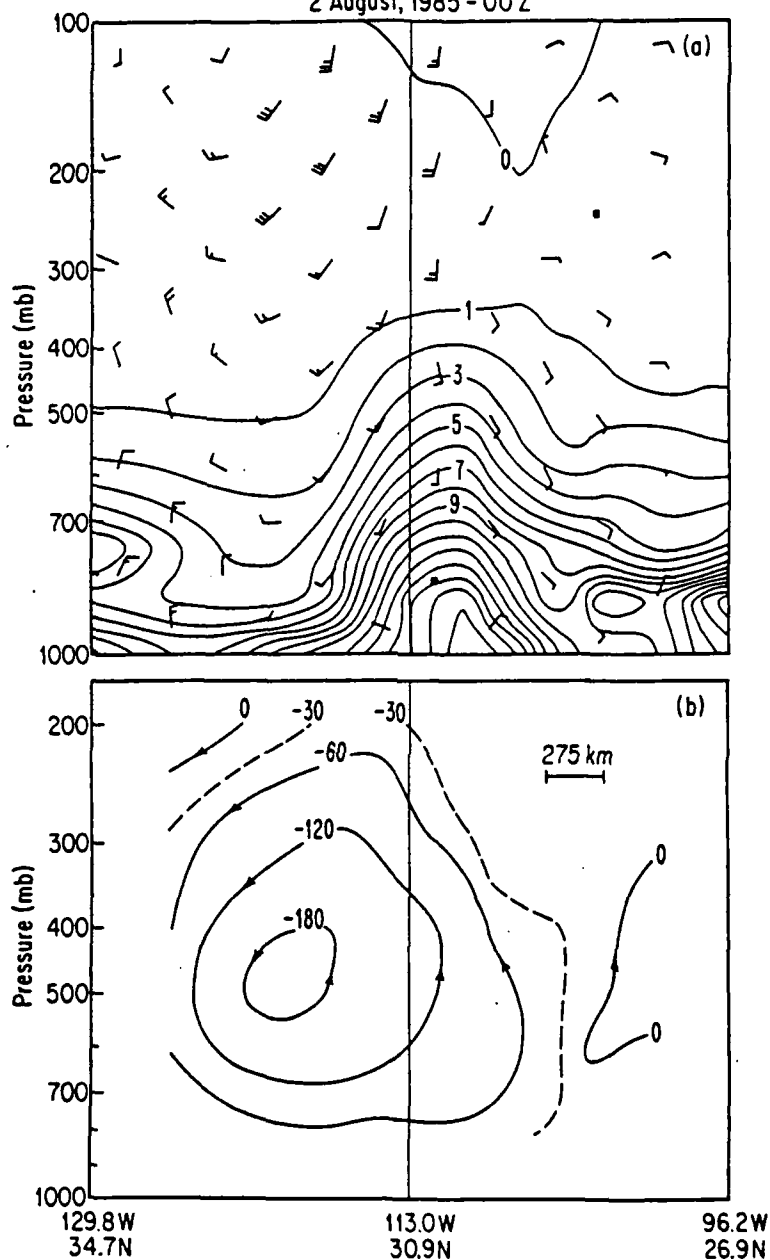


Figure 4.2 Upper figure shows cross section derived from FNOc analysis for 0000Z 2 August 1985. Solid contours are mixing ratio values in g/kg; wind velocities are in standard notation. Cross section runs from northwest of San Diego, CA to the western Gulf of Mexico. The lower figure shows the ageostrophic streamfunction (m·mb/s) computed for the same cross section.

east. This cross section was taken at the same time as the image shown in Figure 4.1.

Several features are apparent in Figure 4.2. There is a deep layer of moisture (surface to 400 mb) just to the east of the boundary, with a rapid transition to much drier air toward the west at all levels except the surface. The edge of the moisture at 400 mb in the cross section compares well with the line separating light from dark in Figure 4.1.

The northwest flow in the lower troposphere over the Pacific and southeast flow over Mexico below 400 mb are consistent with the synoptic scale monsoon circulation described in the Introduction. The strongest winds in the cross section up through 300 mb are only 25 knots and occur about 600 km west of the boundary.

Pronounced deformation in the wind field is suggested near the boundary. The northwest flow to the west of the boundary and southeast to the east indicate confluence toward the boundary. If one assumes these winds are geostrophic, then strong horizontal deformation with the axis of dilatation along the boundary is implied. This deformation flow apparently maintains the sharp moisture contrast

across the boundary and forces the ageostrophic circulation shown in Figure 4.2b and described in Section 4.2. It will be shown later that confluence forces the temperature gradients that are colocated with the moisture gradients.

#### 4.1 Composite cross section of the boundary

A composite description of the boundary was generated to show that a particular cross section is not unique and to produce a mean depiction of the boundary. Although compositing the cross sections smooths the gradients, the resulting wind and temperature fields show significant detail.

For each of the eleven cross sections, the horizontal winds were converted to components  $u$  and  $v$ , parallel (positive into the cross section) and perpendicular (positive toward the left) to the boundary, respectively. Since the cross sections were essentially perpendicular to the boundary, then  $u$  is along the boundary and  $v$  is across the boundary.

The zero  $v$  isotach, which was nearly vertical, was then used to define the location of the boundary. One cross section, in which the zero  $v$  isotach was near the center, was used as a base for the composite grid; each of the remaining cross sections was

overlaid on the base and shifted in the cross-boundary direction until the zero  $v$  isotachs more or less matched. After all the cross sections were overlaid, the data were summed to produce the composite cross section. Thus, the composite boundary is at center of the composite cross section, by definition.

Table 4.1 shows the number of data inputs at each grid point of the composite cross section. The internal 12 of 18 total grid points include data from at least half the cross sections and the middle third of the grid points contain data from all 11 individual cross sections.

Figure 4.3 shows the composite cross sections. The across boundary winds ( $v$ ) in Figure 4.3b show flow toward the boundary from both east and west. Furthermore, the vertical gradients of this component, especially near the boundary are relatively weak, suggesting very weak along boundary temperature gradients. As pointed out earlier, if one assumes the across-boundary flow in Figure 4.3b is geostrophic, then strong horizontal deformation with the axis of dilatation along the boundary axis (here, the zero  $v$  isotach) is suggested.

TABLE 4.1. Data Input at Composite Boundary Grid Points

Grid Point Numbers																		
1	2	3	4	5	6	7	8	9	10	11	12	13	14	15	16	17	18	
X	X	X	X	X	X	X	X	X	X	X	X							
	X	X	X	X	X	X	X	X	X	X	X	X						
		X	X	X	X	X	X	X	X	X	X	X	X					
		X	X	X	X	X	X	X	X	X	X	X	X					
		X	X	X	X	X	X	X	X	X	X	X	X					
			X	X	X	X	X	X	X	X	X	X	X	X				
				X	X	X	X	X	X	X	X	X	X	X	X			
					X	X	X	X	X	X	X	X	X	X	X	X		
						X	X	X	X	X	X	X	X	X	X	X	X	
1	2	5	6	8	10	11	11	11	11	11	11	11	10	9	6	5	3	1
Number of Data at Each Grid Point																		

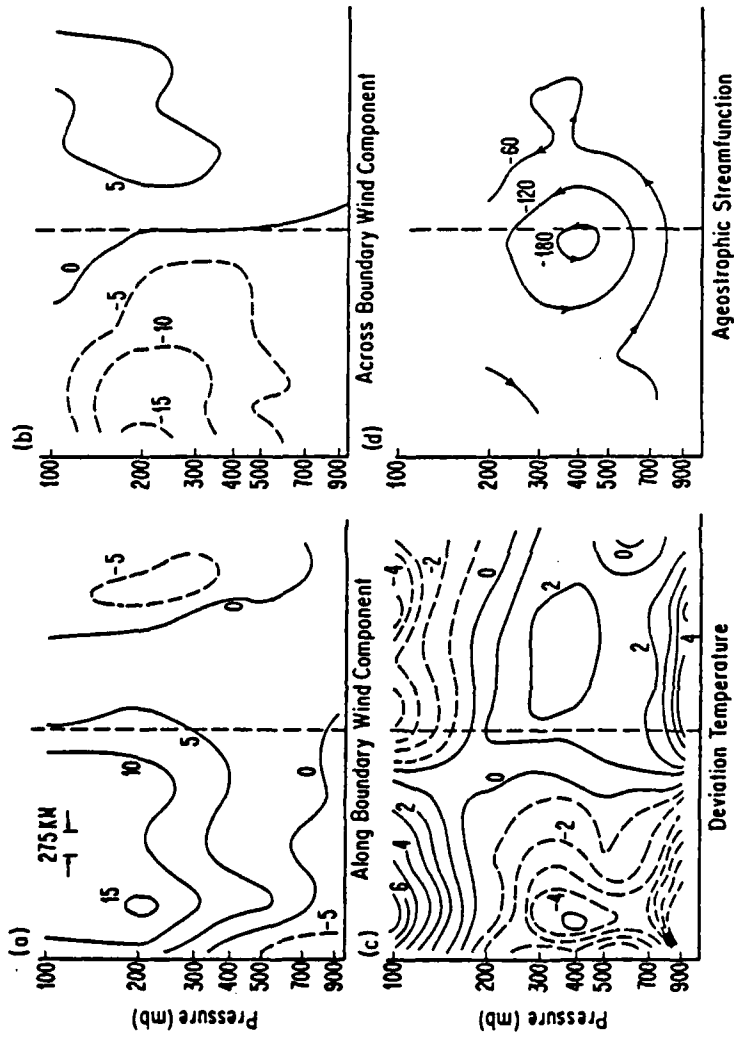


Figure 4.3 Features of the composite boundary: (a) Along-boundary winds ( $u$ ) in m/s; positive flow is into diagram. (b) Cross-boundary winds ( $v$ ) in m/s; positive flow is toward the left in the diagram; zero  $V$  isotach denotes boundary location. (c) Temperature deviations from horizontal average in  $^{\circ}\text{C}$ . (d) Ageostrophic circulation in  $\text{m}\cdot\text{mb}/\text{s}$ . The line of the cross section is the same as Fig. 4.2, although it spans a somewhat larger western-most point in these sectors is toward the left.

Figure 4.3c shows the temperature deviation from a horizontal average. This figure clearly demonstrates that tropospheric temperatures above 700 mb are warmer to the east of the monsoon boundary. Temperature gradients approach  $0.3^{\circ}\text{C}/100\text{ km}$ , which can be compared with mid-latitude fronts, where the overall temperature gradients may approach  $1^{\circ}\text{C}/100\text{ km}$  (locally, especially at the earth's surface, they may be much higher). Note that the very large gradients at the surface represent the contrast between the land (Mexico) and the adjacent cool Pacific.

Above 200 mb, the temperature distribution is reversed, with colder temperatures to the east of the boundary and warmer temperatures to the west. This represents temperatures at the base of the stratosphere, which in summer in this area is generally around 100 mb. The cold temperatures at 100 mb east of the boundary thus indicate a high tropopause, while the warm temperatures to the west indicate a low tropopause and a correspondingly warmer and lower stratosphere. The monsoon boundary, therefore, is also a zone separating a region with a deep troposphere from one with a relatively shallow troposphere.

Figure 4.3c suggests that the bulk of the temperature gradient in the lower troposphere lies to the cold side of the boundary, which was defined as the point where the across boundary wind component goes to zero. This, of course, is the situation with mid-latitude fronts. Also, because the temperature gradients are to the cold side of the boundary, the vertical wind shear is also greatest in this region as demonstrated in Figure 4.3a. Note the jet in the composite cross section (which is generally from the south) is clearly west of the boundary and reaches magnitudes in excess of  $15 \text{ m}\cdot\text{s}^{-1}$ . To the east of the boundary, there is virtually no vertical gradient of the along boundary wind component, suggesting an atmosphere that is nearly barotropic.

#### 4.2 Secondary transverse circulation

The two-dimensional, geostrophic momentum (GM) version of the Sawyer-Eliassen (S-E) equation (Shapiro, 1981) was used to diagnose the transverse ageostrophic circulation associated with the dynamical forcing implied by the wind field in Figures 4.3a and 4.3b. The GM approximation neglects the acceleration of horizontal ageostrophic motions ( $dV_a/dt=0$ ) but retains horizontal and vertical ageostrophic

advections of  $U$ , the along-front geostrophic wind. This version of the S-E equation applies to approximately straight frontal zones governed by the assumption that the cross-front balance of forces is nearly geostrophic. This implies the along-front wind component can be approximated by its geostrophic value ( $u_a = 0$ ) and the ageostrophic circulation is two-dimensional and confined to the transverse plane.

Shapiro (1981) describes the governing equations and assumptions used to derive the GM version of the S-E equation. Besides using the GM approximation and assuming  $u_a = 0$ , he assumes Boussinesq flow and neglects frictional and diabatic processes as well as latitudinal derivatives of the Coriolis parameter. With these assumptions, the governing equations are:

$$\frac{dU}{dt} = \frac{\partial U}{\partial t} + U \frac{\partial U}{\partial x} + (V + v_a) \frac{\partial U}{\partial y} + \omega \frac{\partial U}{\partial p} = f v_a \quad (4.1)$$

$$\frac{dV}{dt} = \frac{\partial V}{\partial t} + (V + v_a) \frac{\partial V}{\partial y} + \omega \frac{\partial V}{\partial p} = 0 \quad (4.2)$$

$$\frac{d\theta}{dt} = \frac{\partial \theta}{\partial t} + U \frac{\partial \theta}{\partial x} + (V + v_a) \frac{\partial \theta}{\partial y} + \omega \frac{\partial \theta}{\partial p} = 0 \quad (4.3)$$

$$\frac{\partial U}{\partial x} + \frac{\partial V}{\partial y} = 0 \quad (4.4)$$

$$m = U - fy \quad (4.5)$$

$$\gamma \equiv \frac{R}{f} \frac{p_0}{p} \frac{c_v}{c_p} \quad (4.6)$$

$$\frac{\partial U}{\partial p} = \frac{\partial m}{\partial p} = \gamma \frac{\partial \theta}{\partial y} ; \quad \frac{\partial V}{\partial p} = -\gamma \frac{\partial \theta}{\partial x} \quad (4.7)$$

$$\frac{\partial v_a}{\partial y} + \frac{\partial \omega}{\partial p} = 0 \quad (4.8)$$

$$v_a = -\frac{\partial \psi}{\partial p} ; \quad \omega = \frac{\partial \psi}{\partial y} \quad (4.9)$$

The respective equations denote along- and cross-front momentum (4.1 and 4.2), thermodynamic energy (4.3), nondivergent geostrophic wind (4.4), geostrophic absolute momentum (4.5), geostrophic thermal wind (4.7), mass continuity (4.8), and secondary circulation velocity components (4.9).

The frontal development equations result from taking  $\partial/\partial y$  of Equation 4.1,  $\gamma \partial/\partial y$  of Equation 4.3 and  $\partial/\partial p$  of Equations 4.1 and 4.3, substituting Equation 4.8, and assuming Boussinesq flow ( $\partial\gamma/\partial p = 0$ ). The adiabatic, frictionless frontal development equations are:

$$\frac{d}{dt} \left( \frac{\partial m}{\partial y} \right) = J_{yp}(m, \omega) \quad (4.10)$$

$$\frac{d}{dt} \left( \frac{\partial m}{\partial p} \right) = -J_{yp}(U, V) - J_{yp}(m, v_a) \quad (4.11)$$

$$\frac{d}{dt} \left( \gamma \frac{\partial \theta}{\partial y} \right) = J_{yp}(U, V) + \gamma J_{yp}(\theta, \omega) \quad (4.12)$$

$$\frac{d}{dt} \left( \frac{\partial \theta}{\partial p} \right) = -J_{yp}(\theta, v_a) \quad (4.13)$$

They give the frontogenesis forcing of the vertical component of vorticity, vertical wind shear, cross-front thermal gradient and static stability, respectively.

The S-E equation results from eliminating the temporal derivatives of Equations 4.11 and 4.12 through Equation 4.7 and inserting Equation 4.9. The S-E equation is:

$$-\gamma \frac{\partial \theta}{\partial p} \frac{\partial^2 \psi}{\partial y^2} + 2 \frac{\partial m}{\partial p} \frac{\partial^2 \psi}{\partial y \partial p} - \frac{\partial m}{\partial y} \frac{\partial^2 \psi}{\partial p^2} = -2J_{yp}(U, V) \quad (4.14)$$

where  $J_{yp}(U, V)$  is the Jacobian and  $y$  is positive toward the colder air. Other symbols are conventional. Equation 4.14 is a linear, second-order elliptic equation of form  $A \psi_{yy} - 2B \psi_{yp} + C \psi_{pp} = Q$ . The coefficients of Equation 4.14 are static stability

( $A = -\gamma \partial \theta / \partial p$ ), baroclinicity ( $B = -\partial m / \partial p = -\gamma \partial \theta / \partial y$ ), and absolute vorticity ( $C = -\partial m / \partial y$ ).

The ellipticity condition,  $AC - B^2 > 0$ , requires the potential vorticity,  $J_{yp}(m, \theta)$  to equal or exceed zero, which was the case for the composite boundary. Since the distributions of  $m$ ,  $\theta$ ,  $U$ , and  $V$  are known and the ellipticity condition is met for the composite boundary, Equation 4.14 can be solved uniquely for the streamfunction provided boundary conditions are specified. The solution, of course, can be fairly sensitive to the choice of boundary conditions on  $\psi$ .

Solutions were computed for Equation 4.14 using both Dirichlet and Neumann boundary conditions and found virtually identical solutions. Note that  $U$  and  $V$  used in Equation 4.14 were, in fact, the observed winds, which included the ageostrophic component. However, these ageostrophic components don't affect the calculation of  $\psi$  from Equation 4.14 because they are much smaller than their geostrophic counterparts. Additionally, the uncertainty in our knowledge of the observed winds from the FNOC cross sections probably exceeds the ageostrophic component values.

Equation 4.14 is solved using sequential overrelaxation (SOR), as described by Haltiner and

Williams (1980). The SOR solution flow is as follows:

1. Input values of coefficients and forcing functions.
2. Input boundary and initial guess data ( $\psi = 0$ ).
3. Calculate

$$\psi^{n+1}(I,J) = \psi^n(I,J) + \frac{\alpha R(I,J)}{2 \frac{A(I,J)}{(\Delta y)^2} + \frac{C(I,J)}{(\Delta p)^2}}$$

where  $\alpha$  is the SOR coefficient and  $R(I,J)$  is the difference scheme of Equation 4.14 minus the forcing function.

4. Iterate until an acceptable level of accuracy is reached.

The forcing function in Equation 4.14 can be broken down into two parts:

$$F1 = -2 \frac{\partial U}{\partial y} \frac{\partial V}{\partial p} \quad (4.15)$$

$$F2 = 2 \frac{\partial U}{\partial p} \frac{\partial V}{\partial y} \quad (4.16)$$

$F1$  is the geostrophic horizontal shear and denotes the effect of cross-front geostrophic wind shear rotating along-front thermal gradients into the cross-front direction.  $F2$  denotes the effect of geostrophic confluence in strengthening cross-front thermal gradients.

Figure 4.3d shows the solution of Equation 4.14 for the total forcing function ( $F_1 + F_2$ ), while Figure 4.4 shows the solutions for  $F_1$  and  $F_2$  separately. Figure 4.4 clearly demonstrates the ageostrophic motion associated with the monsoon boundary is primarily forced by confluence. This should not be surprising since, as noted earlier,  $\partial v / \partial z \approx 0$ ; this implies very weak along boundary temperature gradients and, hence, ageostrophic motions must be forced by confluence. In fact, Equations 4.12 and 4.14 demonstrate that the forcing of the horizontal temperature gradients by geostrophic motions and the forcing of the ageostrophic flow by geostrophic motions are the same. Thus, it can be said that confluence is responsible for maintaining the horizontal gradients that are the monsoon boundary.

The total streamfunction for the composite case (Figure 4.3d) shows a weak direct circulation with ascent on the warm and moist side of the boundary and descent to the west. Figure 4.2b shows the solution to Equation 4.14 for the individual case on 2 August. The solution is very similar to the composite case with ascent to the moist, warm side (east) of the boundary and descent to the west. Note also that the

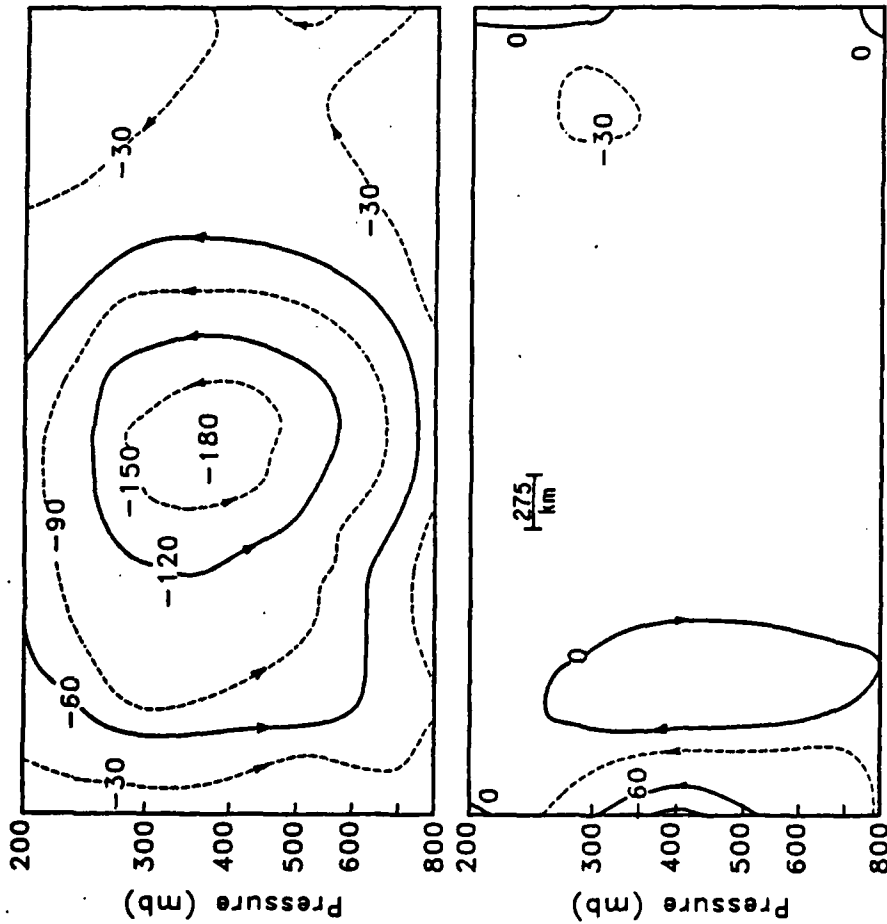


Figure 4.4 Upper figure shows the composite boundary geostrophic streamfunction (m·mb/s) computed for geostrophic confluence (F2). Lower figure shows the composite boundary geostrophic streamfunction (m·mb/s) computed for geostrophic horizontal shear (F1). Dashed lines are negative. Circulation is clockwise around positive maxima.

moisture field in Figure 4.2a clearly reflects the vertical motions implied by the ageostrophic streamfunction, with dry air descending almost to the surface in the subsiding current and a deep layer of moisture in the ascending current.

#### 4.3 Static stability

Figure 4.5 shows representative profiles of potential temperature,  $\theta$ , and equivalent potential temperature,  $\theta_e$ , for regions west of the boundary in the cool, dry air and east of the boundary in the warm, moist air. Note that the Tucson sounding (Figure 3.1) showed substantially less variation of  $\theta$  below 700 mb than seen in the composite boundary. The composited data may be quite different than the actual data from a given location, especially near the surface.

The vertical profile of  $\theta_e$  in the moist air mass is conditionally unstable in the lower and middle troposphere, as is true for the mean tropical sounding (Holton, 1979). This emphasizes the tropical origin of this moist air mass. On the dry side of the boundary, there is a general increase in  $\theta_e$  with height, and thus, with respect to moist processes, the dry side is clearly more stable. On the other hand,

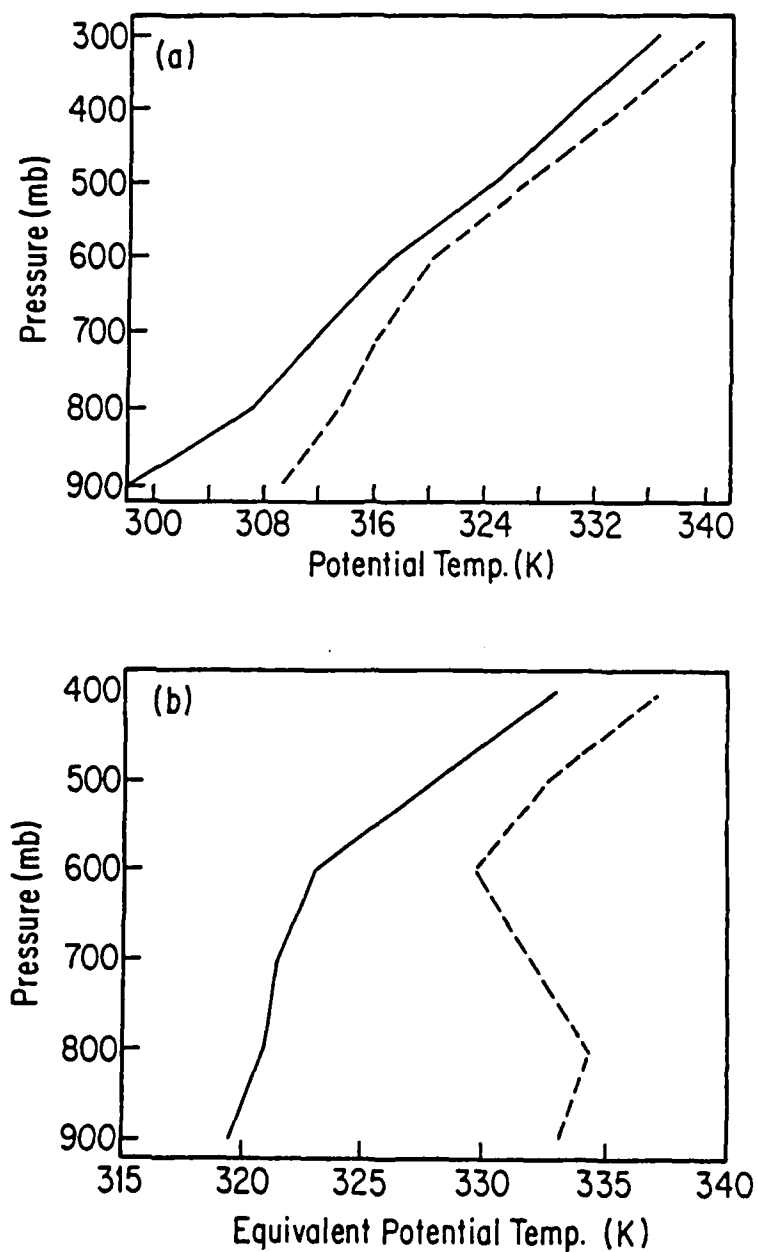


Figure 4.5 Upper figure shows representative profiles of potential temperature ( $^{\circ}\text{K}$ ) on either side of the composite monsoon boundary. Lower figure shows representative profiles of equivalent potential temperature ( $^{\circ}\text{K}$ ) at same locations. Dashed lines indicate moist side of boundary; solid lines indicate dry side of boundary.

with respect to dry processes, the stability of both sides is roughly the same. This is emphasized in Figure 4.5a which shows the distribution of potential temperature on both sides of the boundary. The overall vertical gradient of  $\theta$  is less on the moist side, as we might expect in an atmosphere that has been modified toward a moist adiabatic lapse rate. Figure 4.5b also emphasizes the air on the moist side of the boundary is potentially warmer than that on the dry side. This again demonstrates the moist side of the boundary is the warm side. This needs to be emphasized since, when one witnesses the passage of the boundary at a particular station, little temperature change occurs. In fact, as was noted earlier, the surface may actually cool. The cool air near the surface doesn't show in Figure 4.3 because the compositing process emphasizes the strong surface temperature difference between ocean and land which masks the smaller temperature difference across the boundary.

#### 4.4 Tracer frontogenesis

The dominant feature of the monsoon boundary is the sharp gradient of moisture across the boundary. To investigate the relative strengths of the

mechanisms forcing that sharp gradient, I used a tracer frontogenesis equation derived as follows:

- 1) Assume  $dq/dt=0$  (where  $q$  is defined as mixing ratio), use GM approximation, and neglect frictional forces such that

$$\frac{dq}{dt} = \frac{\partial q}{\partial t} + U \frac{\partial q}{\partial x} + (V + v_a) \frac{\partial q}{\partial y} + \omega \frac{\partial q}{\partial p} \quad (4.17)$$

- 2) Take  $\partial / \partial y$  of Equation 4.17 and substitute from Equation 4.8 yielding

$$\frac{d}{dt} \left( \frac{\partial q}{\partial y} \right) = -J_{xy}(q, U) + J_{yp}(q, \omega) \quad (4.18)$$

- 3) Further simplify by assuming that along-boundary variations in mixing ratio are negligible when compared to cross-boundary variations, yielding

$$\frac{d}{dt} \left( \frac{\partial q}{\partial y} \right) = -\frac{\partial q}{\partial y} \frac{\partial V}{\partial y} + J_{yp}(q, \omega) \quad (4.19)$$

The terms on the right hand side of Equation 4.19 are the confluence and ageostrophic components of the total mixing ratio tracer frontogenesis forcing.

Table 4.2 shows maximum values for total tracer frontogenesis, as well as maximum values of its confluence and ageostrophic components. Negative values imply that the gradient of moisture is becoming stronger with time. As expected, the maximum values occurred at the boundary. The dominant component, as seen in Table 4.2, is confluence strengthening the cross-boundary gradient of moisture. However, the ageostrophic component accounts for roughly 20 percent of the total.

#### 4.5 Comparison with mid-latitude fronts

Table 4.3 compares the maximum velocity component values from the composite monsoon boundary to those Shapiro (1981) computed for a simulated mid-latitude front. For the ageostrophic components, the streamfunction shown in Figure 4.3 was used (computed using Equation 4.9). The most noticeable difference between the flow in the vicinity of the monsoon boundary and Shapiro's front is the strength of the along-front jet. Whereas the maximum along-front wind is  $60 \text{ m}\cdot\text{s}^{-1}$  for the simulated mid-latitude front, the maximum along-front wind for the composite monsoon boundary is only  $15 \text{ m}\cdot\text{s}^{-1}$ . The secondary circulation velocity components show the same comparative strength

TABLE 4.2. Maximum Values of Tracer Frontogenesis Components

---

---

<u>Component</u>	<u>Value</u> ( $10^{-6}$ g/kg/100 km/s)
Total	-1.82
Confluence	-1.48
Ageostrophic	-0.34

---

---

TABLE 4.3. Maximum Values of Velocity Components

Parameter	Monsoon Boundary	Simulated Front
$U$ ( $\text{m}\cdot\text{sec}^{-1}$ )	15	60
$V$ ( $\text{m}\cdot\text{sec}^{-1}$ )	15	16
$\omega$ ( $\text{mb}\cdot\text{day}^{-1}$ )	21	69
$v_a$ ( $\text{m}\cdot\text{sec}^{-1}$ )	1	4

as the along-front wind maxima since the forcing terms are directly proportional to variations in U and V.

Table 4.4 compares maximum values of the forcing by the various Jacobians in Equations 4.10-4.13 for the monsoon boundary and simulated front. The forcing of the monsoon boundary cross-front vorticity and vertical wind shear are only about 10 percent of the simulated frontal values, while the forcing of the monsoon boundary cross-front thermal gradient and static stability are about 25-30 percent of the simulated frontal values.

The magnitude of the flow associated with the monsoon boundary may, in individual situations, be higher than shown in Table 4.3 due to the smoothing inherent in the compositing process. In at least one of the eleven cross sections used for the composite boundary, the maximum value of the vertical motion of the ageostrophic flow exceeded  $40 \text{ mb} \cdot \text{d}^{-1}$  ( $0.5 \text{ cm} \cdot \text{s}^{-1}$ ).

While the monsoon boundary shares many characteristics with a typical mid-latitude front, it generally is not as strong (at least in the cross sections derived from the FNOC forecast models). This is perhaps not surprising since meteorologists rarely, if ever, indicate frontal systems in this region

TABLE 4.4. Maximum Values for Frontogenesis Forcing

Parameter	Monsoon Boundary	Simulated Front
$J(m, v_a)$ ( $10^{-8} m \cdot s^{-2} \cdot mb^{-1}$ )	-39	-360
$J(m, \omega)$ ( $10^{-11} s^{-2}$ )	-5	-50
$-J(\theta, v_a)$ ( $10^{-8} K \cdot mb^{-1} \cdot s^{-1}$ )	27	90
$J(\theta, \omega)$ ( $10^{-8} m \cdot s^{-2} \cdot mb^{-1}$ )	56	160
F2 ( $10^{-8} m \cdot s^{-2} \cdot mb^{-1}$ )	42	150

during the summer months. On the other hand, the magnitude of the flow with the monsoon boundary is on the order of one-fourth the flow of a typical mid-latitude front and may occasionally approach magnitudes typical of middle latitudes. This suggests that not only should the boundary be viewed as a front, but that the possibility of wave formation along this front, similar to mid-latitude cyclogenesis, should also be considered. Chapter 6 presents a case study of a wave disturbance that appears to originate along the monsoon boundary in July 1984. Moore et.al. (1989) actually examine the baroclinic stability of the monsoon boundary. Their results are briefly described in Chapter 6.

## CHAPTER 5

## STRUCTURE OF THE MONSOON BOUNDARY FROM VAS DATA

On 22-23 July 1985, the 500 mb pattern over the southwestern United States and northern Mexico showed two high pressure centers (one over Guadalupe Island and the other centered over Monterrey, Mexico) with a trough between them centered over Arizona and northern Sonora. The surface map indicated a thermal low over Yuma but no analyzed fronts or troughs in Arizona, New Mexico, or northern Mexico. Precipitation occurred over most of northern Arizona and a small area in southeastern Arizona on 22 July and over much of New Mexico on 23 July.

Figure 5.1 shows IR and water vapor images for 22-23 July. The water vapor images show the monsoon boundary running north-south through central Arizona at 0530Z 22 July and near the Arizona-New Mexico border at 0530Z 23 July. Note that there is little convective activity at this evening hour (2230 LST) on either day. The IR images show substantial convective activity at 0000Z on 22 and 23 July, occurring roughly parallel to the monsoon boundary on its eastern side.

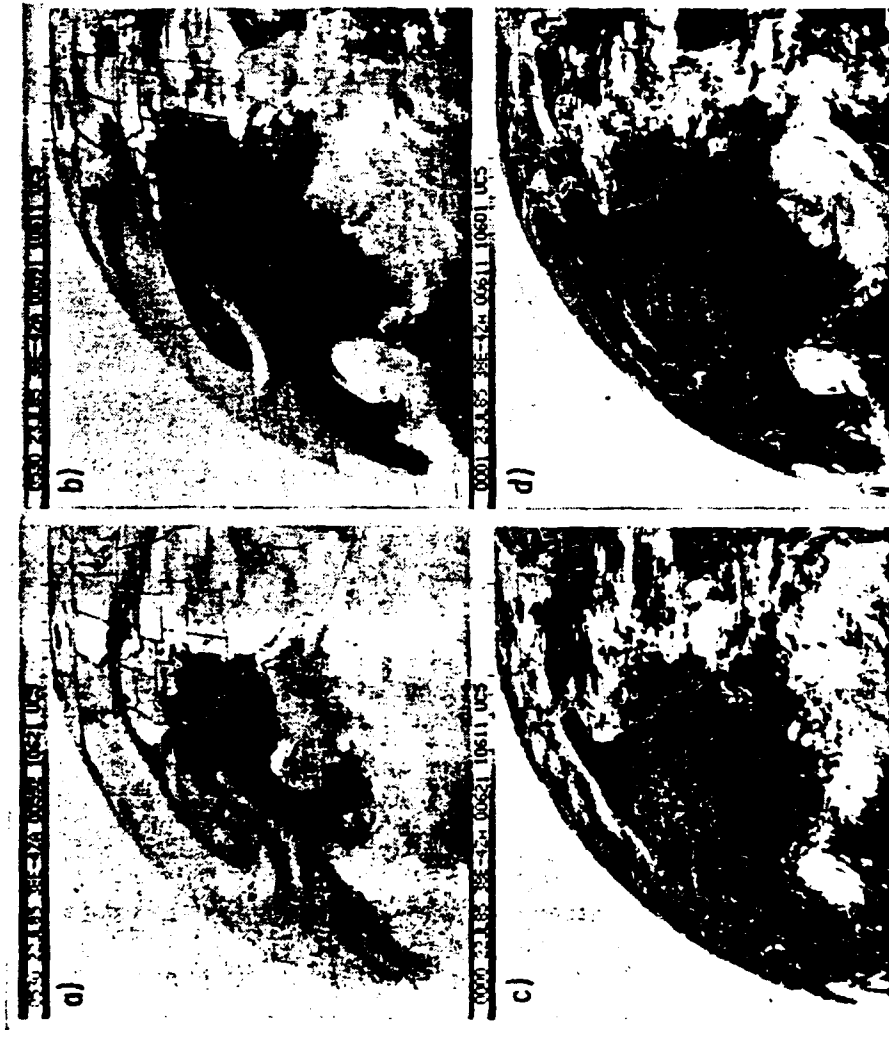


Figure 5.1 (a) GOES 6.7  $\mu\text{m}$  image at 0530Z 22 July 1985. (b) GOES 6.7  $\mu\text{m}$  image at 0530Z 23 July 1985. (c) GOES IR image at 0000Z 22 July 1985. (d) GOES IR image at 0000Z 23 July 1985.

Figure 5.2 shows the lightning strike data for 0000-0238Z, 23 July and the approximate location of the monsoon boundary inferred from the 6.7  $\mu\text{m}$  imagery at that time. The lightning-strike data correlate extremely well with the cloud clusters evident in the Figure 5.1 IR imagery. Both clearly indicate thunderstorms occurring east of the boundary indicated by the 6.7  $\mu\text{m}$  imagery in the moist air. To the west of the boundary where the air is drier, the lightning data indicate an absence of thunderstorms.

Figure 5.3 shows the morning dewpoints at Tucson spanning the period considered above. Although the water vapor imagery in Figure 5.1 shows the monsoon boundary passing over Tucson moving eastward between 0530Z 22 July and 0530Z 23 July, Figure 5.3 indicates lowered surface dewpoints at Tucson occurred 36 hours later, between 1400Z 24 July and 1400Z 25 July. The time lag between boundary passage indicated by the 6.7  $\mu\text{m}$  imagery and suppressed surface dewpoint suggests that either the maximum dry air intrusion at the surface did not occur at the boundary or the boundary at 400 mb was east of the surface position.

VAS soundings were available for only one time during 22 and 23 July, with spatial coverage about

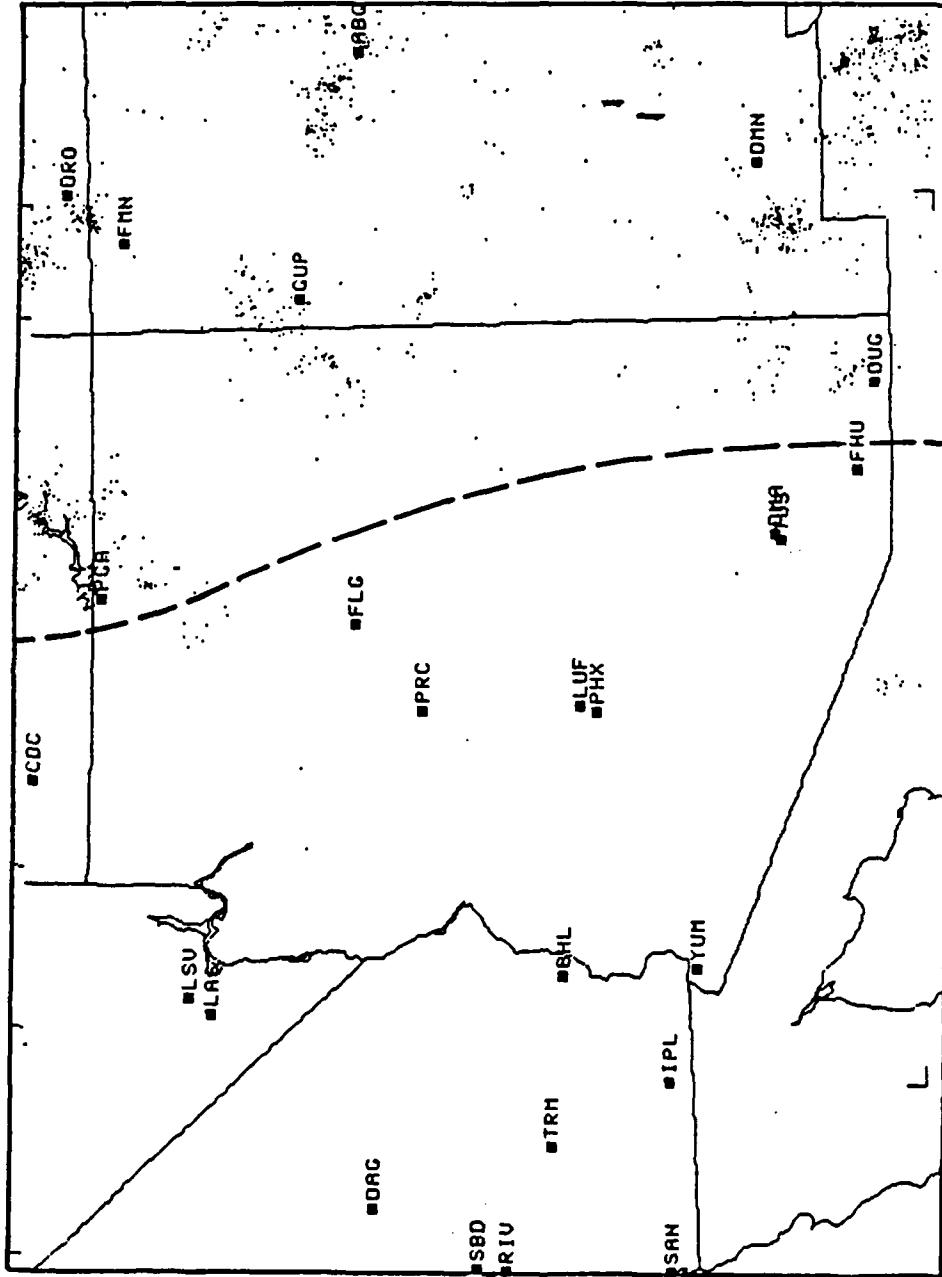


Figure 5.2 Cloud-to-ground lightning-strike locations (dots) for 0000-0238Z, 23 July 1985. Dashed line denotes approximate location of monsoon boundary at that time, inferred from GOES 6.7  $\mu\text{m}$  imagery.

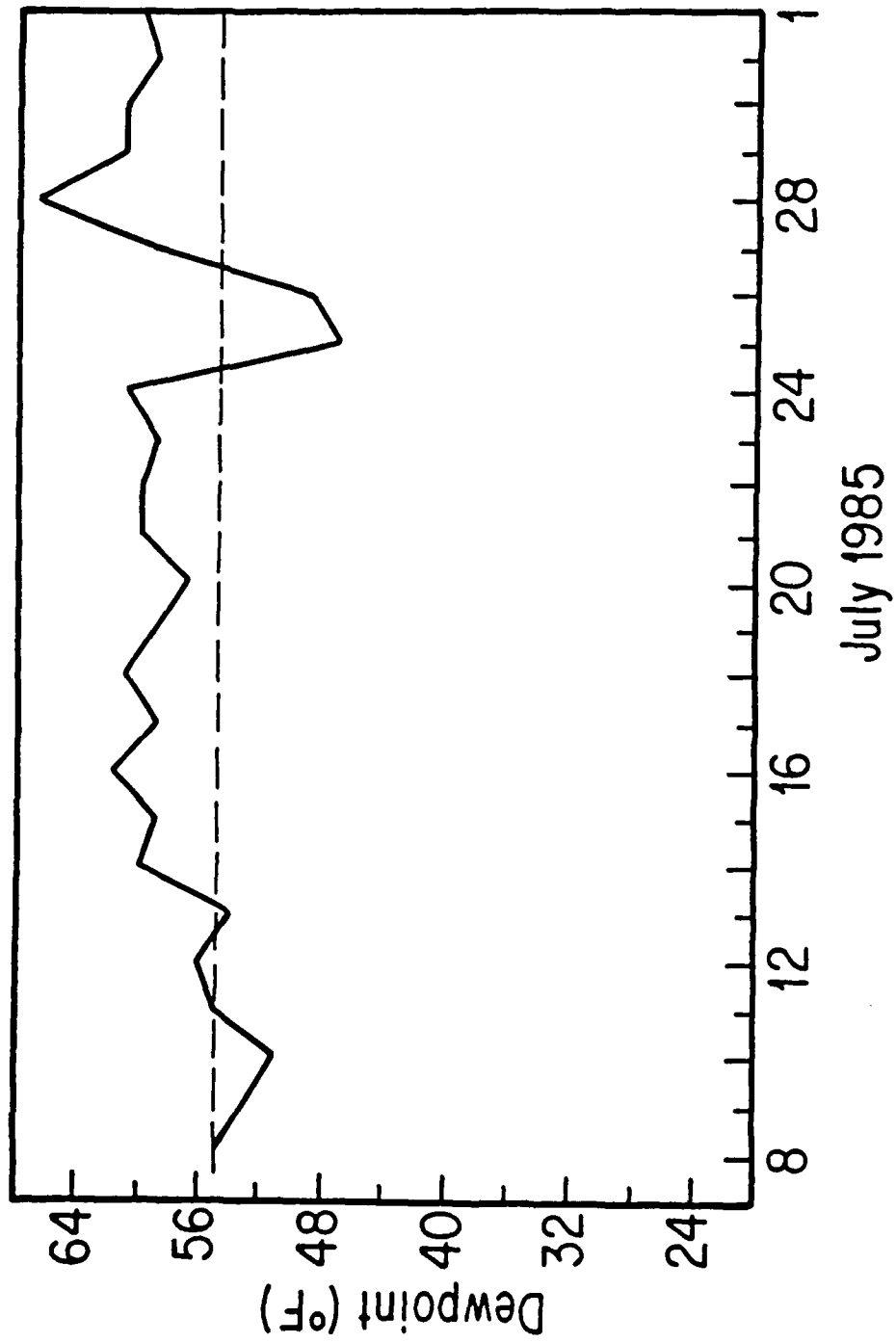


Figure 5.3 Morning (0700 LST) dewpoint (°F) at Tucson for July 1985.

every 75 km. The only area of missing data, due to cloud contamination, occurred over eastern Arizona. The data, however, when presented on horizontal maps was rather noisy. A subjective analysis of individual horizontal maps was performed in order to smooth out the noise. The cross sections shown in this section were then derived from these smoothed maps.

Figure 5.4 shows the subjectively smoothed map of mixing ratio for 400 mb. Note that moist air with mixing ratios greater than  $1 \text{ g}\cdot\text{kg}^{-1}$  are present over New Mexico. There is a very strong gradient of moisture over eastern Arizona with very dry air over western and central Arizona. If the monsoon boundary is placed along the eastern edge of the gradient, it forms a curving line just west of the Arizona-New Mexico border. Note the good agreement with the edge of the light area in the  $6.7 \mu\text{m}$  satellite imagery 12 hours earlier and later, shown in Figure 5.1.

Figure 5.5 gives the cross sections of geopotential height, virtual temperature, and mixing ratio deviations from horizontal average derived from the VAS data for 1648Z 22 July. The cross sections were taken perpendicular to the monsoon boundary

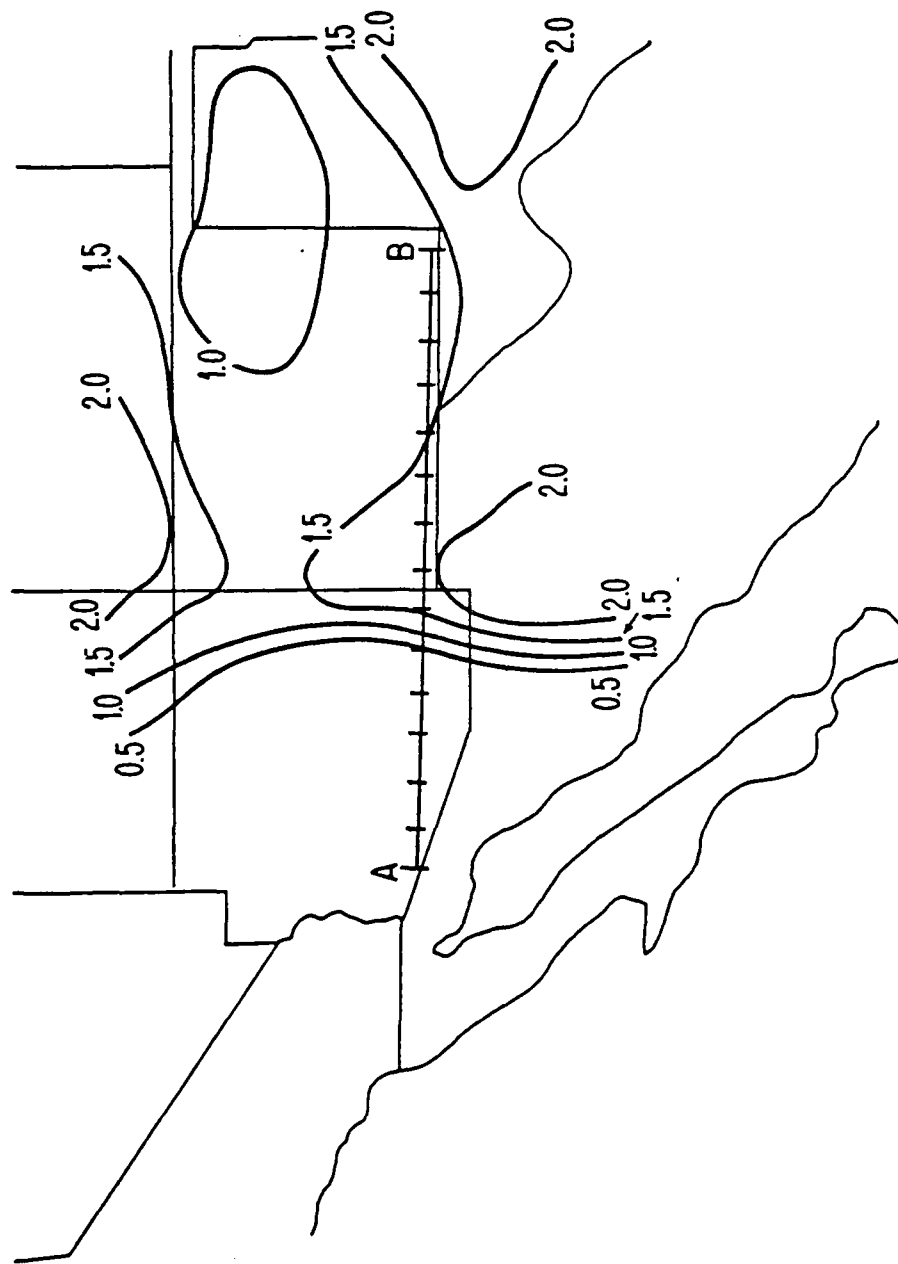
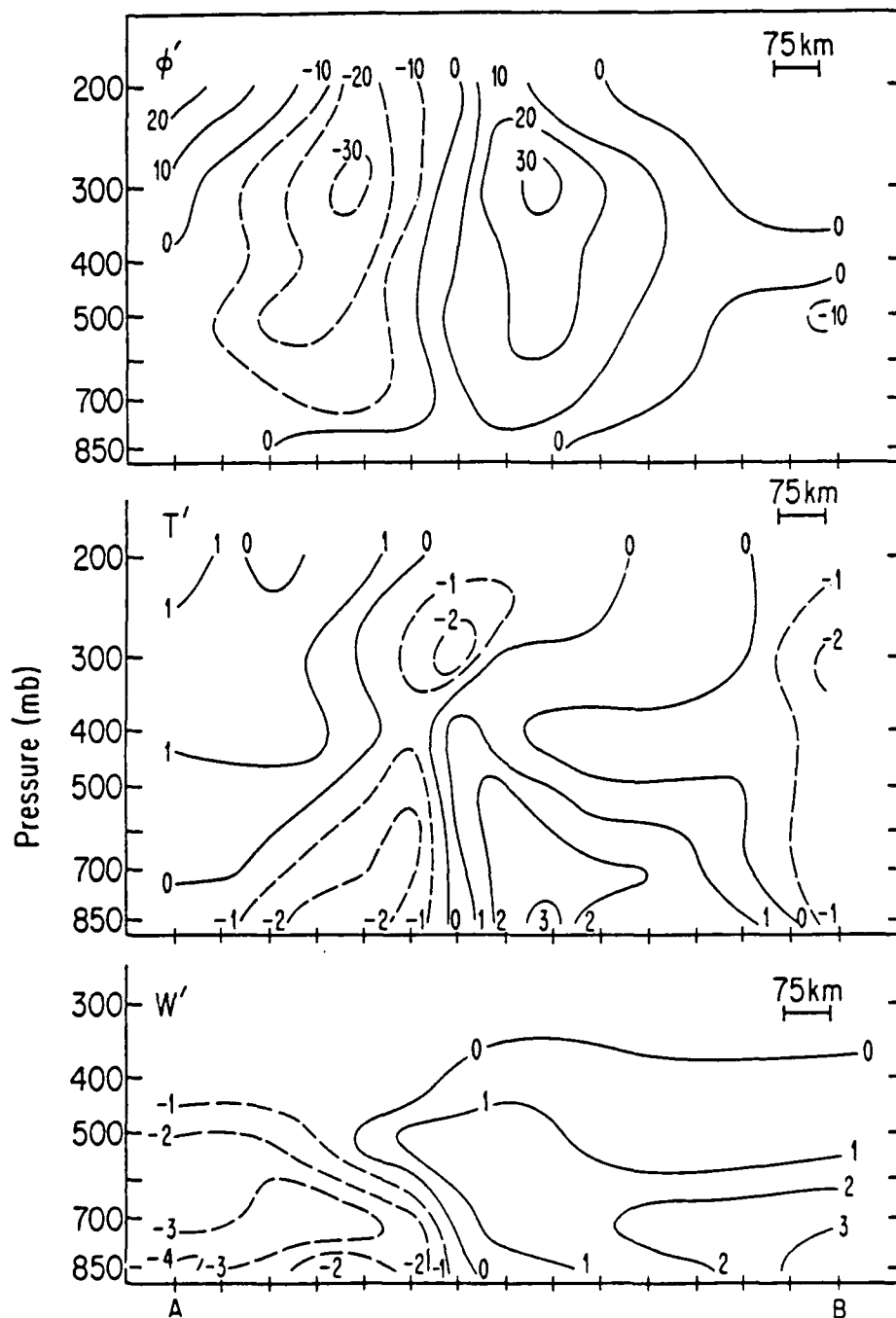


Figure 5.4 400 mb mixing ratio values (g/kg) at 1648Z 22 July 1985, derived from VAS data. Solid line across southern Arizona and New Mexico is trace of cross section for Figure 5.5.



**Figure 5.5** Cross sections of the deviations from the horizontal average for the trace depicted in Fig. 5.4 at 1648Z 22 July 1985. (a) Geopotential height (60m intervals). (b) Virtual temperature ( $^{\circ}\text{C}$ ). (c) Mixing ratio (g/kg). Dashed lines denote negative values.

across Arizona and New Mexico at about  $32.5^{\circ}\text{N}$ . The position of this cross section is noted in Figure 5.4. Note that large horizontal gradients of temperature and moisture exist just to the east of a line extending along the Arizona-New Mexico border, which is the monsoon boundary indicated in Figure 5.2. Note also that the cross sections of temperature and moisture produced from the VAS data are similar to the cross sections shown in Chapter 3 (Figure 4.3). That is, the air on the moist side of the boundary is generally warmer than the air on the dry side, at least near the surface. Thus, the general structure of the boundary that has already been described is present in the instantaneous cross-sections taken with VAS data.

What the VAS data demonstrates (that can only be hinted at in the analyses of the previous sections) is the strength of the gradients in the vicinity of the boundary. While the composite cross section showed maximum temperature gradients of  $0.3^{\circ}\text{C}/100\text{ km}$ , the VAS data suggests gradients in excess of  $3.0^{\circ}\text{C}/100\text{ km}$ , an order of magnitude greater. Mixing ratio gradients from the VAS soundings reach  $3\text{ g/kg}/100\text{ km}$ . The

magnitudes of these gradients approaches or equals those found in many mid-latitude fronts.

The geopotential height perturbation cross section indicates a deep trough extending through the depth of the troposphere about 100 km to the west (on the dry side) of the region of large moisture gradient. This trough is also a similar distance west of the temperature gradient. Recall from Figure 3.2d that when the moisture gradient passed over Tucson in 1984 it was preceded by a minimum of pressure by about 24 hours. Thus, both figures suggest that the main surface pressure trough is just to the dry side of the strong moisture gradients.

The significance of this is not clear, especially since the usual model of a front places both the moisture and temperature gradients on the cool side of the trough. Precisely where the gradients will occur, however, depends on the details of the dynamical forcing of the front, including the ageostrophic secondary circulation. Cloud track wind data from satellite images was not available for this particular case study. There were few clouds present in the early morning hours; the afternoon clouds were cumuliform, with little apparent motion and, thus,

could not be used. A comparison of RAOB winds to gradient winds computed from VAS temperature and height fields showed large directional errors, rendering VAS derived geostrophic winds useless as was noted earlier. Therefore, the lack of wind data prevented computing the transverse circulation about the boundary.

In spite of the lack of wind data, one surmises there is a stronger secondary circulation about the monsoon boundary in this case, as compared with the composite boundary in Chapter 4, simply because the temperature gradient is stronger. This secondary circulation may well enhance daytime convective activity. Note the apparent line of thunderstorms parallel to the monsoon boundary in Figure 5.1c,d. However, as seen in Figure 5.1a,b, the secondary circulation is not strong enough to initiate or sustain thunderstorm development in the absence of solar heating.

## CHAPTER 6

## DISTURBANCES ASSOCIATED WITH THE MONSOON BOUNDARY

In Chapter 4, the similarity of the monsoon boundary to mid-latitude fronts was discussed and the possibility of wave formation along the boundary was suggested. In fact, the wind shear depicted in Figure 4.2 suggested that the composite boundary may be unstable to baroclinic or barotropic processes. In Chapter 3, the utility of 6.7  $\mu\text{m}$  imagery in locating the monsoon boundary was shown.

The imagery for the summers of 1984 and 1985 was examined, looking for examples of possible wave development along or disturbances associated with the monsoon boundary. In this chapter, two such examples are described: a) an apparent wave development along the monsoon boundary that occurred over Baja California in early July 1984 and b) an apparent easterly wave that interacted with the monsoon boundary over northern Mexico in August 1985. Additionally, results from Moore et al (1989), who conducted a linear stability analysis of the composite

monsoon boundary, are compared to and contrasted with the first example.

#### 6.1 Disturbance originating along the boundary

On 1-2 July 1984, the 500 mb pattern over the southwestern United States showed a high pressure ridge extending from California through Utah, Arizona, and New Mexico and into western Texas. A low center and inverted trough were situated over northern Baja. The surface map indicated a thermal low over California but no analyzed fronts in the desert Southwest. Precipitation occurred over the southern two-thirds of Arizona, much of New Mexico, and extreme southern California on 1 July; precipitation was scattered over the Mogollon Rim and southeastern Arizona and the southern half of New Mexico on 2 July.

Figure 6.1, a sequence of  $6.7 \mu\text{m}$  water vapor images spanning the 36 hour period 2315Z 30 June to 1115Z 2 July 1984 for the above synoptic discussion, illustrates the wave development possible along the monsoon boundary. At 2315Z 30 June, Figure 6.1 displays the monsoon boundary extending from southern California southward through the northern part of the Gulf of California and shows the beginning of wave development along the boundary. Throughout the next



Figure 6.1 A 36 hour sequence of GOES 6.7  $\mu\text{m}$  images (2315Z, 30 June - 1115Z, 2 July 1984) showing development of disturbance along monsoon boundary over southern Baja California.

24 hours, Figure 6.1 suggests cyclonic circulation as drier air appears to move into northern Sonora and moisture appears to extend through southern California and southwestward to  $30^{\circ}\text{N}$ ,  $120^{\circ}\text{W}$ . By 1115Z 2 July, the wave appears much like a mid-latitude occluded cyclone, with an apparent low pressure center at 400 mb situated near  $30^{\circ}\text{N}$ ,  $120^{\circ}\text{W}$ .

Figure 6.2 depicts the apparent cyclone at 1115Z 2 July 1984 in greater detail and displays three distinct features that suggest the similarity of this disturbance to a mid-latitude wave cyclone developing along a frontal boundary. First, note the extension of a dry slot into the northwest quadrant of the apparent low near 30 N, 120 W. This dry slot extension is typical of mature, occluded mid-latitude cyclones. Second, there is a sharp line separating upper level moist and dry air extending from the low eastward across southern California and northern Arizona. Visible imagery, not shown here, shows a distinct front-like cloud band coincident with this upper level moisture boundary. Third, note the presence of a similar moisture boundary extending southward from the low along the western Mexican coast.



Figure 6.2 GOES 6.7  $\mu\text{m}$  image at 1115Z, 2 July 1984.

Figure 6.3 is a visible GOES image, taken three hours after Figure 6.2, showing a front-like cloud feature roughly coincident with the southward extending moisture boundary evident in Figure 6.2. Figure 6.3 indicates that the front-like cloud band is composed almost entirely of convective clouds. Thunderstorms formed along both front-like cloud features on the afternoon and evening of 1 and 2 July 1984.

The presence of this convection was confirmed by lightning strike data available for the afternoon of 2 July 1984. Figure 6.4 displays that data for 1800-1900Z 2 July over the southwestern U.S. Despite the scatter evident in this data, note the clustering of lightning strikes over southern Nevada, northern Arizona, and western New Mexico. These clusters appear to be associated with the eastward extending cloud feature described above. Unfortunately, the limited range of the BLM lightning detection network did not allow detection of cloud-to-ground lightning strikes in northern Mexico along the southward extending front-like cloud feature.

VAS retrievals and cloud track winds were available at three times for this case study: 2018Z 1



Figure 6.3 GOES visible image at 1415Z, 2 July 1984.

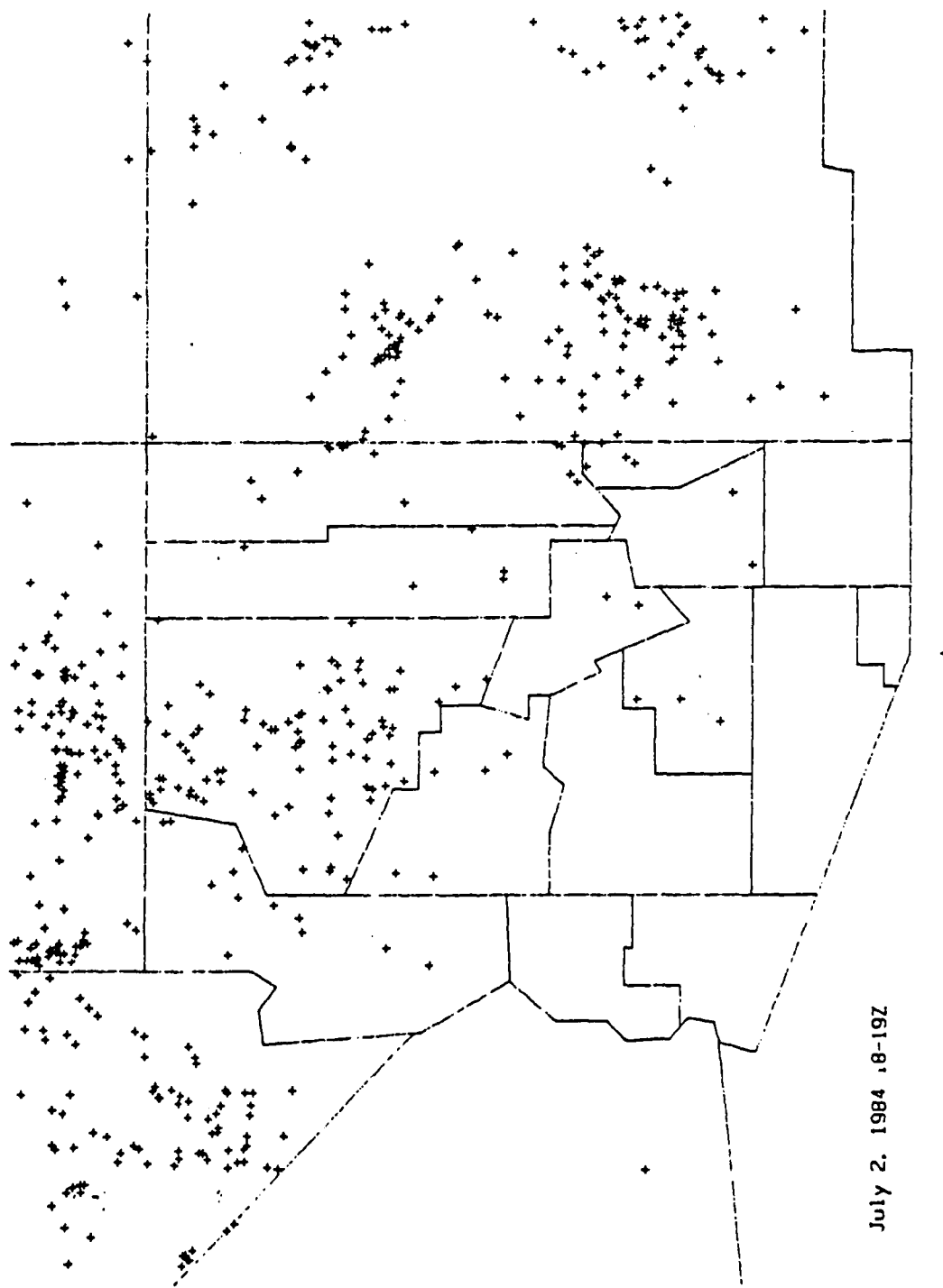


Figure 6.4 Cloud-to-ground lightning strike data for 1800-1900Z, 2 July 1984.

July, 0218Z 2 July and 1418Z 2 July. However, the VAS data at the first two times were limited due to extensive cloudiness over the area of interest. Therefore, only the VAS data at 1418Z 2 July was used. Table 6.1 shows differences between the rawinsonde and VAS derived winds similar to those in Table 3.1. In particular, there were significant directional errors. For the San Diego VAS/RAOB comparison, the wind direction difference was 160 degrees at 200 mb; instances of wind direction differences greater than 100 degrees also occurred for the Tucson VAS/RAOB comparison. Therefore, VAS-derived winds were not used. Although there was also noise present in the temperature, moisture, and geopotential height comparisons, the VAS/RAOB differences were comparatively much smaller and the gradients provided useful information.

The VAS temperature, moisture, and geopotential height fields were obtained on horizontal maps at the mandatory constant pressure levels. Again, as described in Chapter 5, the data were noisy and required subjective analysis to smooth out the noise. Figure 6.5 shows the subjectively smoothed maps of geopotential height at 400 and 700 mb for 1418Z 2

TABLE 6.1. VAS Retrieval/RAOB Comparisons

VAS Data: 1418Z 2 July 1984 RAOBS: 1200Z 2 July 1984				
San Diego VAS - RAOB				
P(mb)	T(°C)	TD(°C)	Z(m)	Wind Direction(Degrees)
Sfc	-1	-3	-	-
850	-6	1	-32	140
700	3	-2	-39	80
500	0	5	-12	-10
400	-2	0	-18	-20
300	-2	-14	-38	-10
200	-2	-	-53	160
Tucson VAS - RAOB				
P(mb)	T(°C)	TD(°C)	Z(m)	Wind Direction(Degrees)
Sfc	0	0	-	-
850	-1	-1	-1	-110
700	3	-1	2	60
500	2	14	35	50
400	-2	-3	38	40
300	-4	-9	-4	110
200	-2	-	-36	20
Guaymas VAS - RAOB				
P(mb)	T(°C)	TD(°C)	Z(m)	Wind Direction(Degrees)
850	1	-1	2	90
700	4	7	28	30
500	0	-13	38	70

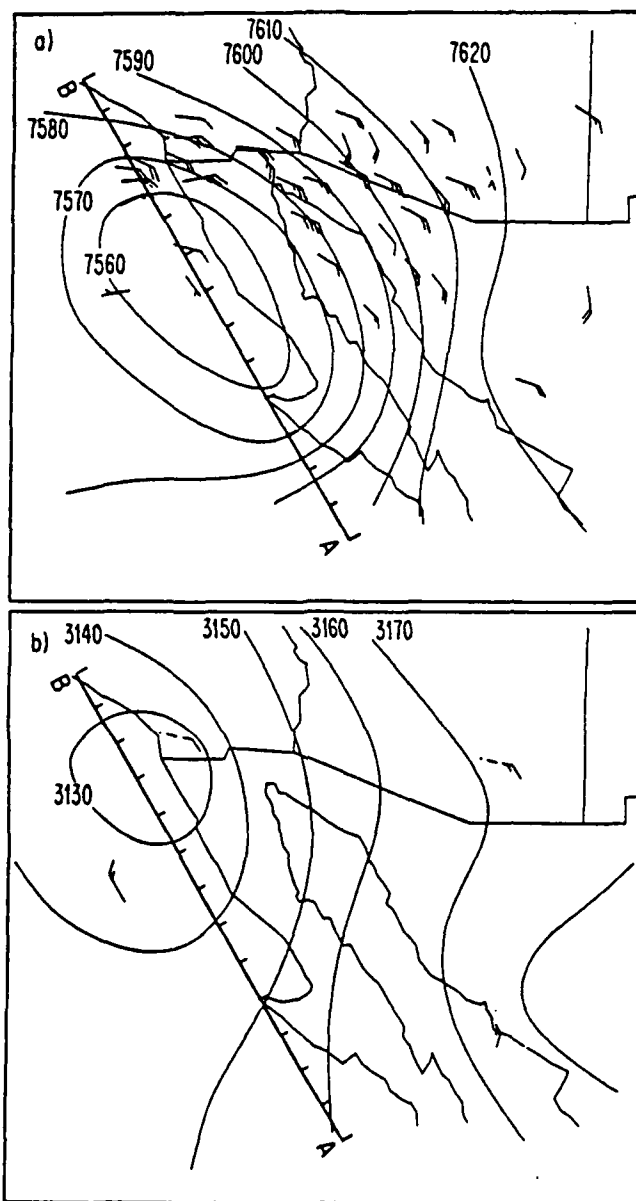


Figure 6.5 Smoothed maps of geopotential height (m) at 1418Z, 2 July 1984, derived from VAS data, for a) 400 mb and b) 700 mb. Cloud track wind (solid wind barbs) data are also plotted. The heavy solid line denoted B-A is the trace of the cross section depicted in Figure 6.6.

July. Additionally, Figure 6.5 shows the closest coincident cloud track wind and rawinsonde data used. These wind data, along with the VAS-derived geopotential height gradients, were used interactively to produce the final geopotential height fields. This synergistic approach in reducing the noise in the geopotential height fields, using the strength of the VAS data (gradient fields) and the accuracy of the wind directions from the rawinsonde data, provided the best possible subjective analysis.

Figure 6.5a indicates a closed low south of San Diego and west of Baja California at 400 mb. This position agrees well with that inferred from the Figure 6.1 water vapor imagery. Figure 6.5b also shows a closed low at 700 mb. But, when compared to 400 mb, the geopotential gradients are substantially weaker and the low is located further to the north-northwest. Also, Figure 6.5b indicates a trough across southern California and southern Arizona, in close proximity to the front-like cloud feature seen in Figure 6.3.

Figure 6.6 shows a cross section of geopotential height deviations from horizontal average at 1418Z 2 July. The trace of the cross section is seen in Figure

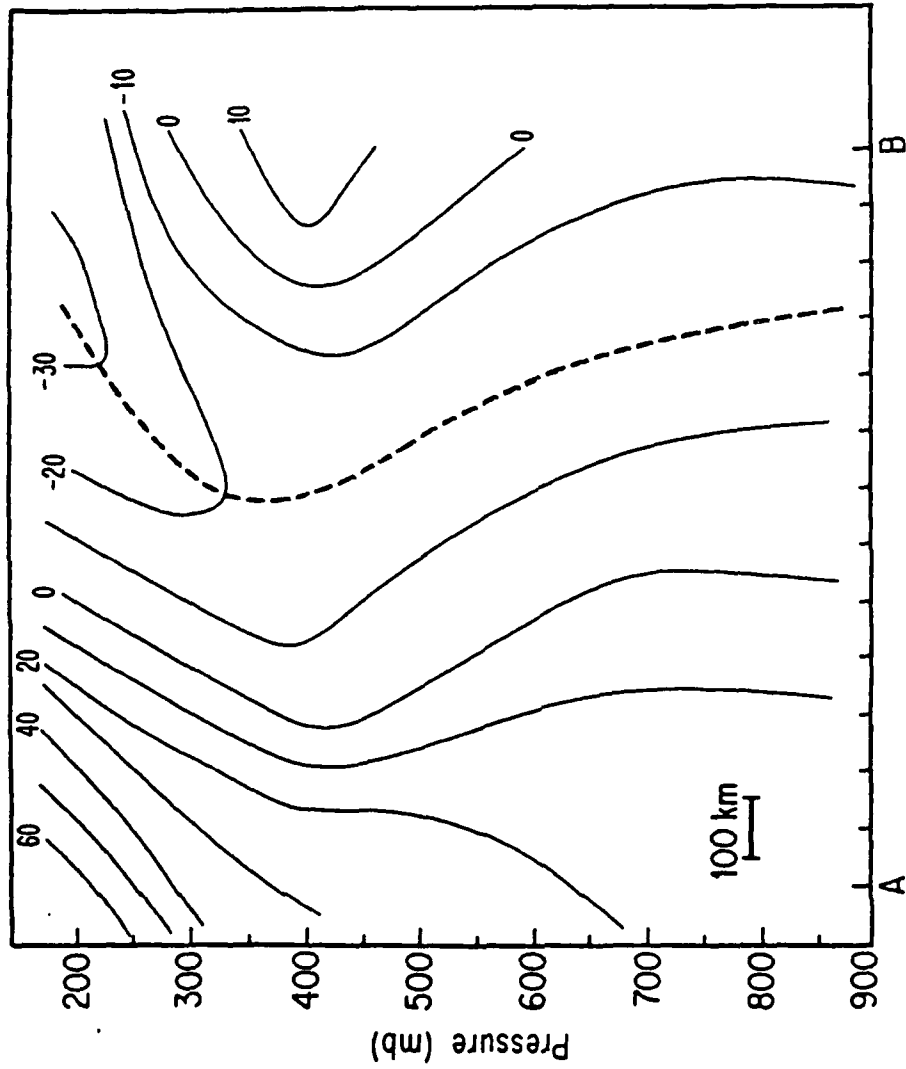


Figure 6.6 Cross section of geopotential height deviation from horizontal average obtained from VAS data at 1418Z, 2 July 1984. Actual trace of cross section is shown in Figure 6.5. The dashed line indicates the trough axis.

6.5, placing it roughly parallel to the monsoon boundary and through the cyclonic swirl seen in Figure 6.2. Figure 6.6 was constructed using the smoothed maps of geopotential height at mandatory pressure levels from 850 to 200 mb (two of which are seen in Figure 6.5). Note the tilt of the trough axis in Figure 6.6. From 850 to 400 mb, the trough is weak but tilts into the along-boundary wind (directed from A to B in Figure 6.6), which is suggestive of a baroclinic wave. However, the maximum geopotential perturbations occur at 200 to 300 mb. Recall from Figure 4.3 that the horizontal wind shear for the composite boundary is greatest at 200 to 300 mb. This suggests that, although both baroclinic and barotropic energy sources are present, barotropic processes dominate for this case.

Figure 6.7 displays an east-west cross section of moisture and temperature deviations from horizontal average at 1418Z 2 July. The cross section runs roughly along  $28^{\circ}\text{N}$ , south of the circulation center (Figure 6.2) and extending eastward to the front-like feature (extending southward from this center) apparent in Figure 6.3. Near the surface, Figure 6.7 shows the warmer temperatures and higher mixing ratios

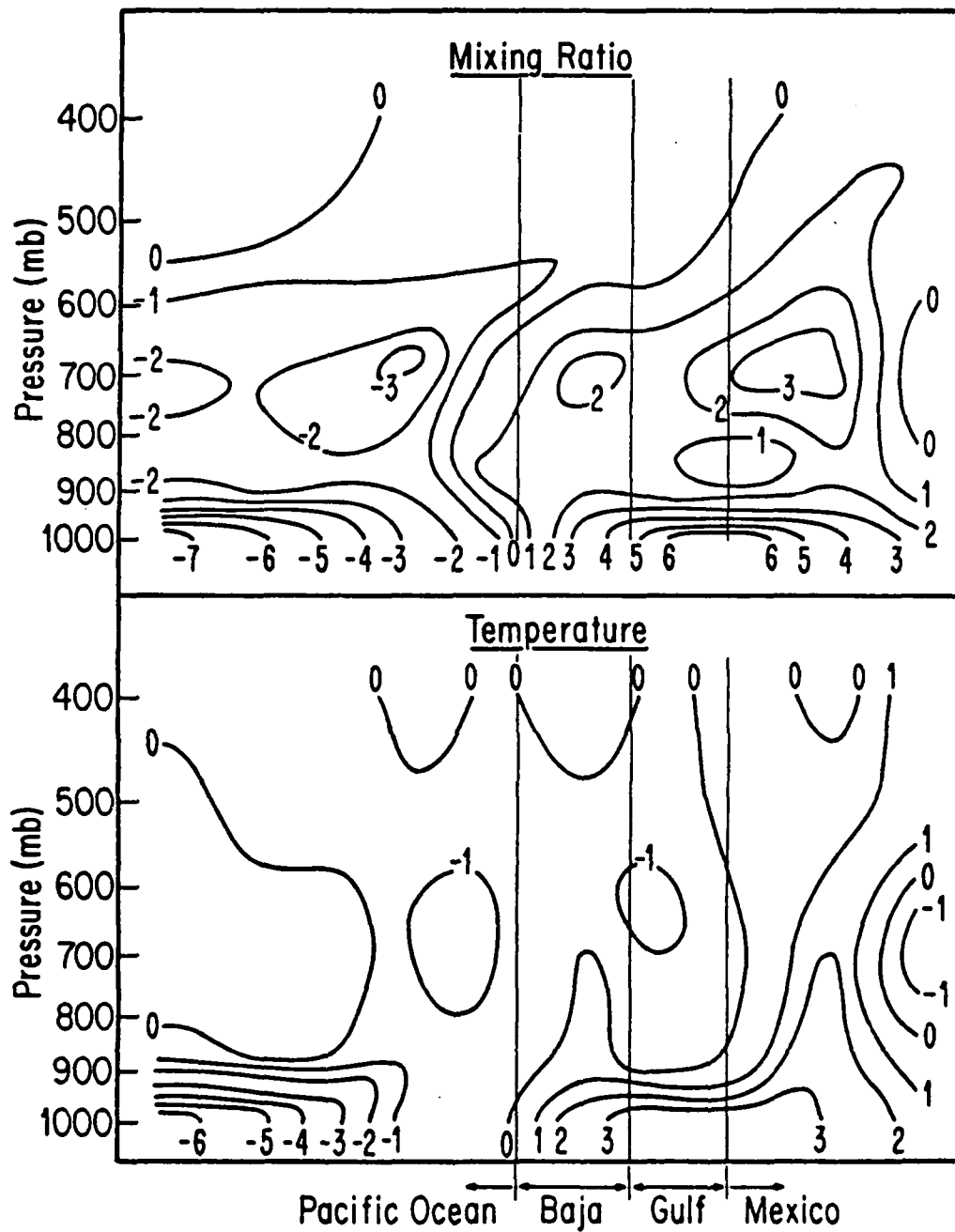


Figure 6.7 Cross sections of the deviations from the horizontal average of mixing ratio (g/kg) and temperature ( $^{\circ}$ K) along 28 N from about  $119^{\circ}$ - $109^{\circ}$ W at 1418Z 2 July 1984. Data derived from VAS retrievals.

expected over the Gulf of California compared to the eastern Pacific Ocean. Above 850 mb, the mixing ratio deviations clearly show two positive moisture maxima: one over Baja California at 700 mb and the other over the Mexican coast at 700 mb. The positive moisture deviations over the Mexican coast extend up to 400 mb, which coincides nicely with the moisture pattern depicted in Figure 6.2. The strongest moisture gradient, though, lies along the western Baja California coast.

The temperature deviations are much less definitive. As described above, the temperature deviations near the surface show the influence of the cold eastern Pacific Ocean and the warm Baja California, Gulf of California, and Mexican land mass. Above the surface layer, there seems to be little horizontal temperature gradient except near the Mexican coast and Baja California, coinciding with the region of elevated moisture. The strong temperature gradient at the far right edge of Figure 6.7 is probably noise, induced by cloud contamination from the front-like cloud feature evident in Figure 6.3.

Figure 6.7 is in many ways similar to Figure 4.2. The region of elevated moisture suggests that

ascending motion is present in that area while strong descent exists further west. Unfortunately, VAS-derived winds were not good enough to calculate the ageostrophic circulation, as was done for Figure 4.2. However, Figure 6.7 suggests a frontal boundary may be present along the Mexican coast, although the temperature gradient is weak. The mixing ratio deviations would suggest the boundary, or front, associated with the circulation feature may indeed be along the Mexican coast in the mid-troposphere (in agreement with the placement of a trough by the VAS-derived geopotential height map in Figure 6.6) if there were a suitable explanation for the secondary maxima over Baja California.

One could infer from Figures 6.2 and 6.5 that two different flow regimes exist over Baja California and western Mexico in the lower troposphere. The flow over Baja California in the lower troposphere appears to be west-southwesterly, with cool moist air mixed being advected into the region from the Pacific Ocean. On the other hand, the flow over western Mexico is southeasterly, with warm moist air apparently advected into the region. With this explanation for the double maxima in the mixing ratio deviations, there is at

least some plausibility for the presence of a weak front along the Mexican coast.

Moore et al (1989) subsequently examined the stability of the composite monsoon boundary, using a linear stability model, to determine the boundary's susceptibility to barotropic or baroclinic processes. They found that, indeed, the boundary is unstable, with maximum growth rates about  $0.4 \text{ d}^{-1}$  and wave lengths of maximum instability about 1200-1500 km. However, unlike the observed disturbance seen in Figure 6.6, the maximum amplitude of the most unstable wave in the linear analysis was at the earth's surface.

They also estimated the wavelength and growth rate of the observed disturbance from Figure 6.1, defining the amplitude of the wave as half the length of the protrusion of moist air evident in the 6.7  $\mu\text{m}$  imagery. From 1115Z 1 July to 1115Z 2 July, the amplitude of the observed wave grew from about 1200 km to about 1500 km. Using a finite difference form of the equation for growth rate ( $d \ln A / dt$ ), they determined the growth rate of the observed wave to also be about  $0.4 \text{ d}^{-1}$ .

The results of the linear analysis do not preclude other unstable modes from existing for the composite boundary. The linear analysis can only depict the most unstable wave for a given mean state and cannot depict non linear barotropic effects. Additionally, the linear analysis will not account for disturbances that do not develop in situ but interact with the boundary as a result of the flow regime. However, this section does show that disturbances do exist along the monsoon boundary, that the disturbances have a profound impact on the area's weather, and that the monsoon boundary is unstable enough to support wave development in the same period as observed in Figure 6.1.

#### 6.2 Disturbance interacting with the monsoon boundary

In the mid-latitudes, short wave troughs moving through long wave troughs frequently interact with frontal boundaries and support wave cyclone development. By analogy, one could envision the same scenario for the monsoon boundary when viewing the flow regime depicted in Figure 1.1. As easterly waves travel along the southern extent of the Atlantic High, the southeasterly flow can cause them to eventually interact with the monsoon boundary.

In this section, an example of just such a disturbance identified in satellite imagery is described. Figures 6.8-6.10 show a disturbance advected in the monsoon circulation that directly affects Tucson's weather. Figure 6.8 shows an apparent easterly wave, originating west of Yucatan, moving into southcentral Mexico and interacting with the northern portion of the Intertropical Convergence Zone (ITCZ). In Figure 6.9, a portion of that disturbance appears to move northward along the western Mexican coast toward south-eastern Arizona and southwestern New Mexico. By 0600Z 1 August 1985, the disturbance covers all northern Sonora, eastern Arizona, and western New Mexico. Figure 6.10 shows the original disturbance initiating substantial thunderstorm activity in Colorado and a second disturbance affecting western New Mexico.

Figure 4.1 places the monsoon boundary through the Gulf of California at 0000Z 2 August 1985. Consequently, one possible explanation of wave growth is that the easterly wave may have initiated a disturbance along the monsoon boundary. In any case, the disturbance appears to double in horizontal extent in less than 24 hours (Figure 6.9). Unfortunately,

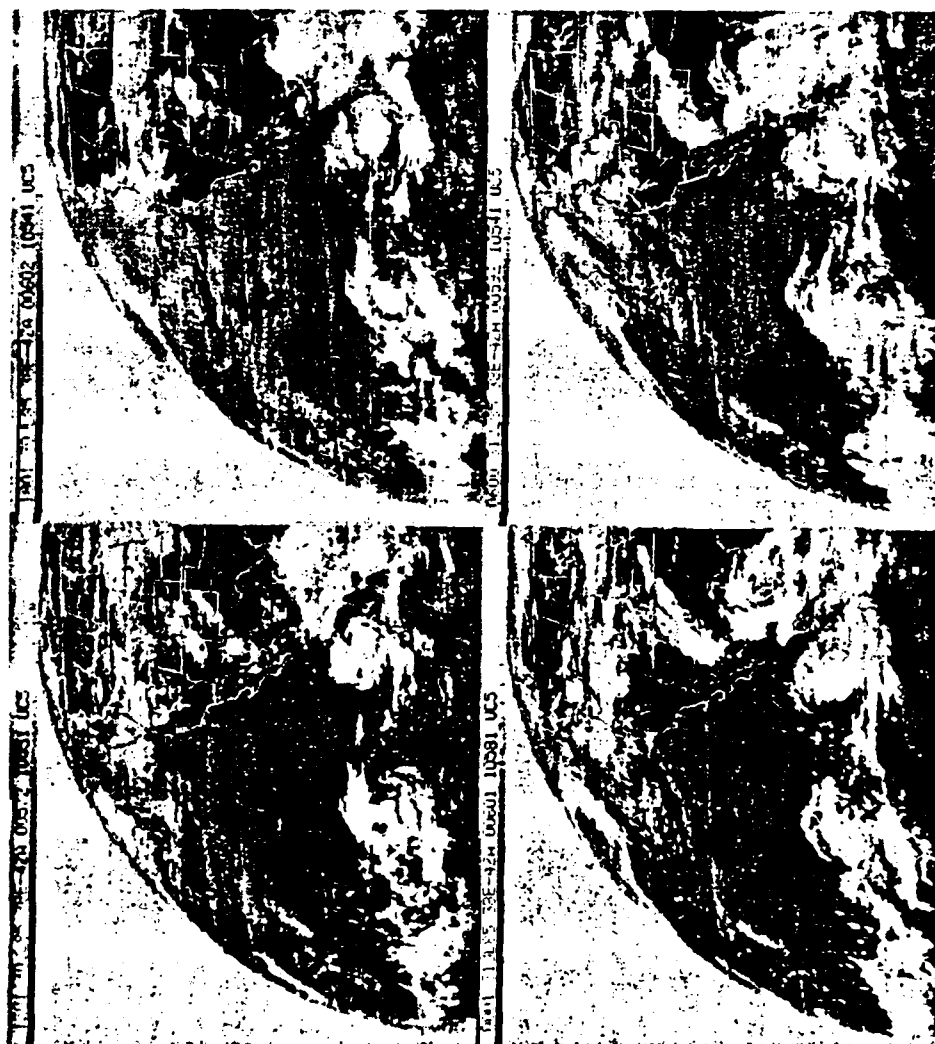


Figure 6.8 SIX-hourly GOES IR images: 1200Z 30 July  
- 0600Z 31 July 1985.

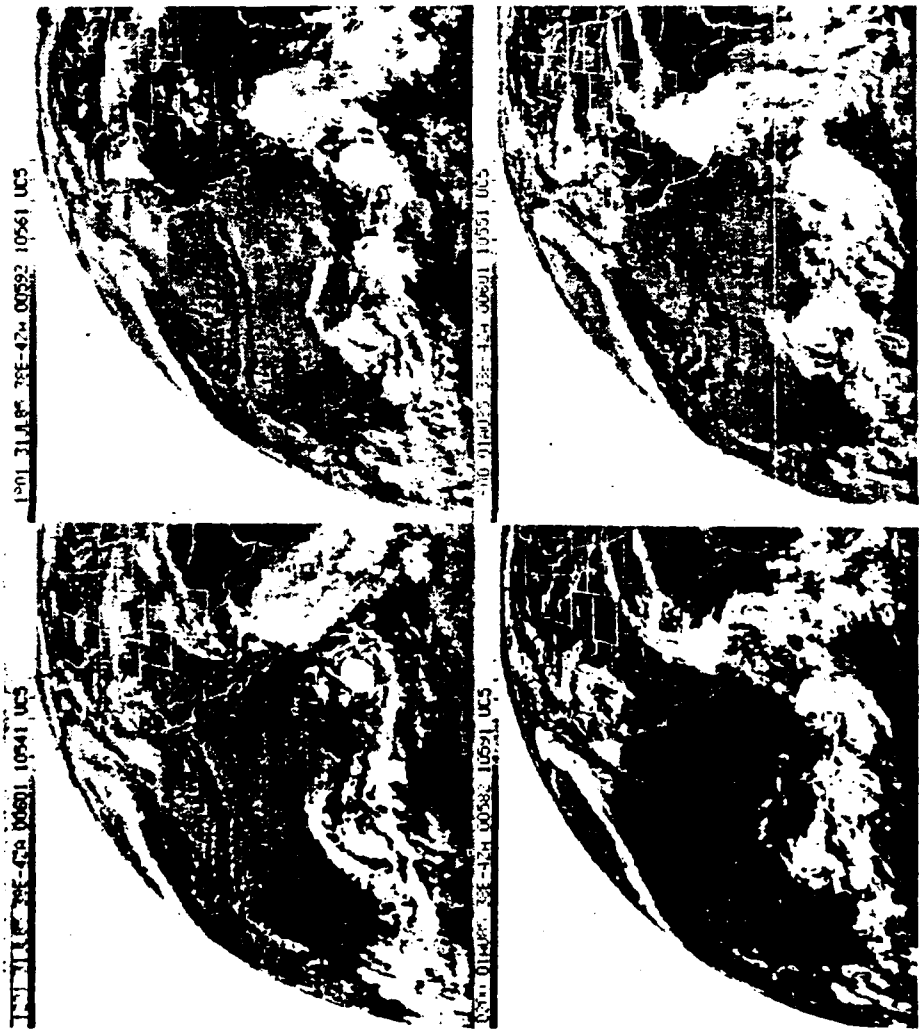


Figure 6.9 Six-hourly GOES IR images: 1200Z 31 July  
- 0600Z 1 August 1985.

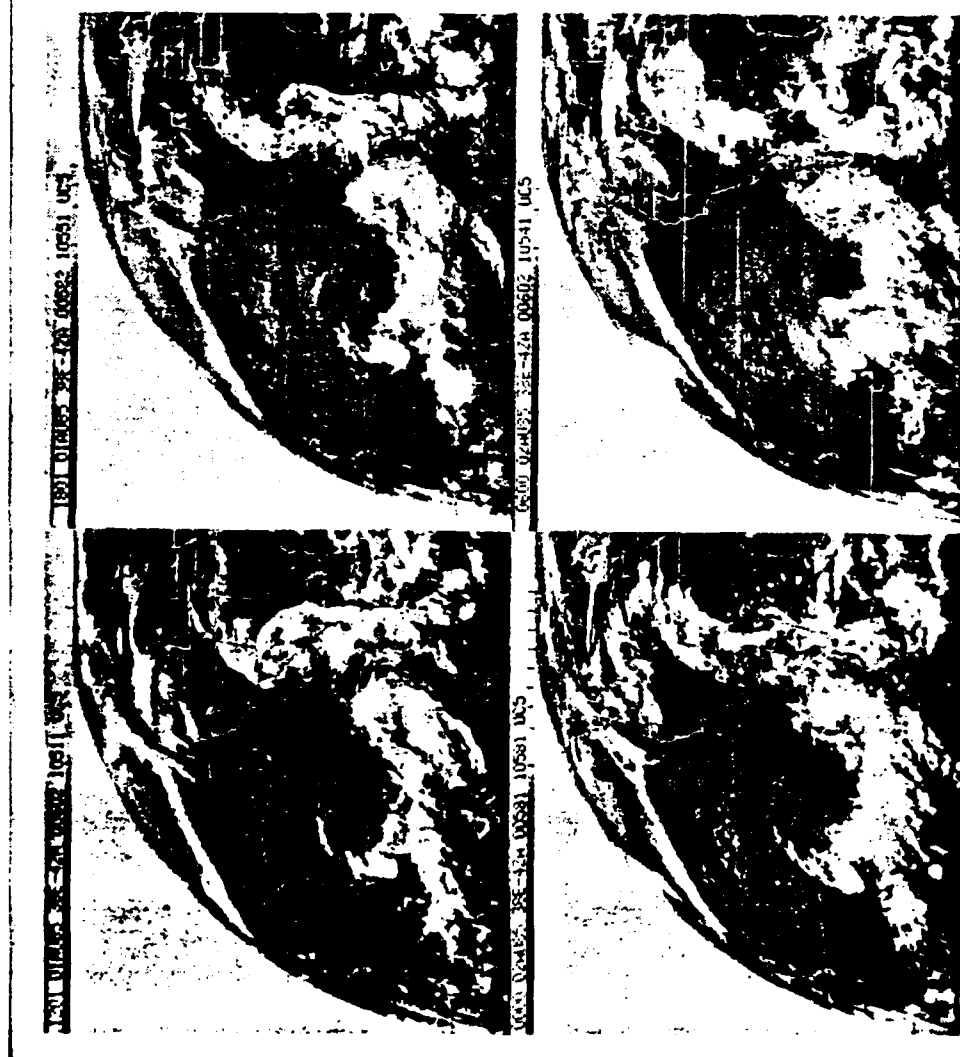


Figure 6.10 Six-hourly GOES IR images: 1200Z 1 August - 0600Z 2 August 1985.

the substantial cloud cover associated with the disturbance seen in Figures 6.8-6.10 prevented using VAS data to examine its structure. However, those figures do show the utility of satellite images in depicting the origin of disturbances that have the potential to affect the desert Southwest during monsoon season.

### 6.3 Conclusions

In Figures 4.2 and 4.3, the horizontal and vertical shear in the wind field suggested that the composite boundary may be unstable to barotropic or baroclinic disturbances. Moore et al (1989), in performing a linear stability analysis of the composite monsoon boundary, demonstrated that the monsoon boundary is unstable and could support unstable barotropic and/or baroclinic waves.

The existence of two disturbances that appear to interact with that boundary has been shown. The first example showed a disturbance that appeared to initiate along the boundary, to display growth rates predicted by the linear analysis, and to impact the weather in the desert Southwest. The second example showed a disturbance from outside the region that appeared to grow when it interacted with the monsoon boundary.

The features of the monsoon boundary and its affect on the observed disturbance show a striking similarity to mid-latitude frontal boundaries and their interaction with mid-latitude wave cyclones.

## CHAPTER 7

## SUMMARY AND RECOMMENDATIONS FOR FUTURE RESEARCH

By compositing cross sections taken from the initial conditions of the FNOC analysis for 1985, a mean depiction of the temperature and wind structure of the Arizona monsoon boundary and surrounding environment was obtained, allowing the boundary's structure and some of its dynamics to be described. The frontal nature of the boundary was evident in examining the moisture, virtual temperature, and wind velocity fields. The boundary, defined as coincident with the  $v=0$  isotach, was the eastern edge of a sharp transition zone to lower values of mixing ratio and somewhat cooler temperatures.

The structure of the boundary illustrated in the composite cross section is also clearly present in similar cross sections produced by other means. For example, a time-height section constructed at the time the boundary passed through Tucson showed an almost identical structure, even though this section was for the previous year. A similar structure was also suggested using soundings from VAS data. Thus, Figure

4.3 provides a good picture of the average structure of the monsoon boundary.

In most respects, the Arizona monsoon boundary resembles a mid-latitude front forced almost purely by confluence. This forcing produces an ageostrophic circulation that is direct and that gives weak ascent on the warm, moist side of the boundary. The gradients and flow associated with the composite boundary are considerably weaker (by a factor of 4) than those associated with strong mid-latitude fronts. However, the cross section taken using VAS data does suggest that, at times, the strength of the boundary approaches that of mid-latitude fronts.

Note, I am reluctant to call the monsoon boundary a front (despite many frontal similarities) because of the weakness of the temperature gradient. However, there is a strong contrast in the two air masses on either side of the monsoon boundary, especially in moisture and wind. Additionally, although the temperature gradient is weak, the bulk of the gradient lies to the cool side of the boundary, a property also common to mid-latitude fronts.

Since mid-latitude fronts are ultimately responsible for the cyclones of middle latitudes, the

role this front-like system may play in the development of disturbances in the southwestern United States during the summer was subsequently examined. The wind shear depicted in Figure 4.2 suggests that the composite boundary may be unstable to baroclinic or barotropic processes. Hence, disturbances developing along the boundary are a distinct possibility.

An apparent example of this type of disturbance was described in Chapter 6, showing the utility of 6.7  $\mu\text{m}$  imagery in identifying disturbance growth along the monsoon boundary. Figure 6.1 shows the rapidity of that growth; within 36 hours, the disturbance grew to resemble a mature, occluded mid-latitude cyclone, with an apparent low pressure center situated over northern Baja California. GOES visible and IR images show front-like cloud features extending eastward and southward from the low and lightning strike data indicate convective activity occurring along those features. Smoothed maps of geopotential height derived from VAS data and wind data (both cloud track and RAOB derived) depict a cyclonic circulation south of San Diego along the Baja California coast. A cross section of geopotential height deviations from

horizontal average along a line approximately at the zero  $v$  isotach shows the vertical axis of low pressure sloping into the shear of the along-boundary winds from the surface to  $\approx 500$  mb. However, above 400 mb, the axis tilts out of the shear; additionally, the disturbance appears to be strongest from 200-350 mb. The wavelength of the disturbance is  $\approx 1200-1500$  km and its growth rate is  $\approx 0.40$   $d^{-1}$ . Lastly, a cross section of mixing ratio and temperature deviations from horizontal average, derived from VAS data, through the southern part of the disturbance appears to support the front-like nature of the cloud feature extending southward into Mexico from the low pressure center.

Moore et.al. (1989) subsequently examined the barotropic/baroclinic stability of the monsoon boundary. They found that, in fact, the boundary is unstable with maximum growth rates between 0.4 and 0.6  $d^{-1}$  at a wavelength of 1200 km and the most unstable wave confined below 700 mb. Although the linear analysis and the observed disturbance discussed in Chapter 6 did not agree as to energy source, one can still make several observations. The data presented in Chapter 6 clearly shows that cyclone-like

circulation systems do occur along the monsoon boundary. As seen on National Weather Service daily weather maps in the summer, this observation is not readily accepted or depicted. Moore et.al. (1989) show that the boundary is unstable enough for waves to grow in 24-48 hours (similar to the observed wave growth rate). Finally, the two analyses show that different types of disturbances may exist at various times or, as Figure 6.6 suggests, at the same time.

Strengths and weaknesses of the non-conventional data used were readily apparent. The satellite imagery, especially 6.7  $\mu\text{m}$  water vapor imagery, were extremely useful in initially suggesting the location of the monsoon boundary and locating disturbances along the boundary and within the monsoon circulation. There was also excellent consistency between the GOES 6.7  $\mu\text{m}$  imagery and VAS moisture gradient fields.

However, the VAS data, although useful for depicting gradients, were quite noisy and routinely required some subjective analysis to adequately depict the information content. Unfortunately, at no time were the VAS winds accurate enough for use.

Quite clearly, more research is required to more fully understand the dynamics and structure of the

monsoon boundary and associated disturbances. The influence of topography (elevated heat source) in the formation of severe thunderstorms in the monsoon circulation needs considerable attention and is, in fact the topic of current research at the Institute of Atmospheric Physics. Effects of latent heat release (from thunderstorms in the moist air) and radiational heating on the gradients of temperature and wind across the boundary need to be studied.

Continued improvements in data acquisition are needed for future research of the monsoon circulation and associated disturbances. Passive remote sensing techniques cannot provide detailed vertical resolution because of the broadness of the weighting functions. The use of ground or spaceborne active sensors offers the best hope for improving vertical resolution. Doppler lidar and radar techniques can provide the detailed vertical profiles of temperature, moisture, and wind necessary to accurately specify disturbance structure. At present, though, the number of active sensors is rather limited. However, the selective use of a wind profiler, as described by Arnold (1985), during the monsoon season could provide a detailed

description of winds and vertical motion across the monsoon boundary.

A combined IR/microwave sounding system is useful for specifying structure in areas that contain clouds. The TIROS Operational Sounder (TOVS) on the current polar orbiting NOAA satellites contains microwave and IR sensors. However, the temporal resolution of the data is poor: six hour sampling interval at best with two polar orbiters. A combination of VAS and TOVS soundings is possible but TOVS soundings for the cases reviewed in Chapters 5 and 6 were not available. Future case study selection should be made with joint availability of VAS and TOVS data in mind.

Despite the limitations of passive radiometry, future work with passive observations will be enhanced because of the launch of GOES 7 in February 1987 and the projected improvements in the next generation GOES, scheduled for launch in 1990. With the launch of GOES 7, there are now two geosynchronous meteorological satellites with VAS capability, significantly enhancing data availability. The next generation GOES will contain an advanced imager with three new spectral channels, IR spatial resolution twice as good as now, and an independent sounder that

measures 19 wavelengths instead of 12. However, the increase in channels does not solve the problem of the lack of vertical resolution due the breadth of the weighting functions.

## LIST OF REFERENCES

- Arnold, J.E., 1985: A comparison between Doppler wind profiles and high resolution Jimosphere/Windsonde data. Proceedings of the Conf. on Aerospace and Range Meteorology, Huntsville, AL, 27-29 Aug 1985.
- Battan, L.J., 1984: Fundamentals of Meteorology. Prentice-Hall, 304 pp.
- Birkenheuer, D. and J. Snook, 1985: A review of the VAS assessment during the 1985 PROFS summer exercise. NOAA Tech Memo ERL ESG-19.
- Brenner, I.S., 1973: A surge of maritime tropical air-Gulf of California to the southwestern United States. NOAA Tech Memo NWS WR88.
- Bryson, R.A. and W.P. Lowry, 1955: Synoptic climatology of the Arizona summer precipitation singularity. Bull. Amer. Meteor. Soc., 36, 329-339.
- Bryson, R.A., 1957: Some factors in Tucson summer rainfall. Technical Reports on the Meteorology and Climatology of Arid Regions, No. 4, Institute of Atmospheric Physics, University of Arizona.
- Bryson, R.A. and F.K. Hare, 1974: The Climates of North America. World Survey of Climatology, Vol. 11, Elsevier Scientific Publishing Company, Amsterdam-London-New York, pp. 1-45.
- Fuelberg, H.E. and P.J. Meyer, 1986: An analysis of mesoscale VAS retrievals using statistical structure functions. J. Climate Appl. Meteor., 25, 59-76.
- Hales, J.E., Jr., 1974: Southwestern United States summer monsoon source-Gulf of Mexico or Pacific Ocean? J. Appl. Met., 13, 331-342.
- Haltiner, G.J. and R.T. Williams, 1980: Numerical Prediction and Dynamic Meteorology. John Wiley & Sons, 477 pp.

## LIST OF REFERENCES--Continued

- Hayden, C.M. and A.J. Schreiner, 1984: Real time meteorological applications of the geostationary satellite sounder on GOES-6: Battling the computer, code, and clock. Recent Advances in Civil Space Remote Sensing, SPIE, Vol. 481, 100-107.
- Hill, C.K. and R.E. Turner, 1983: NASA's AVE/VAS program. Bull. Amer. Meteor. Soc., 64, 796-797.
- Holton, J.R., 1979: An Introduction to Dynamic Meteorology. Academic Press, New York, 391 pp.
- Huschke, R.E., (Ed.), 1959: Glossary of Meteorology. Amer. Meteor. Soc., 638 pp.
- Jedlovec, G.J., 1985: An evaluation and comparison of vertical profile data from the VISSR Atmospheric Sounder (VAS). J. Atm. Ocean. Tech., 2, 559-581.
- Jurwitz, L., 1953: Arizona's two-season rainfall pattern. Weatherwise, 6, 96-99.
- Krider, E.P., R.C. Noggle, A.E. Pifer, and D.L. Vance, 1980: Lightning direction-finding systems for forest fire detection. Bull. Amer. Meteor. Soc., 61, 980-986.
- Menzel, W.P., W.L. Smith, and T.R. Stewart, 1983: Improved cloud motion wind vector and altitude assignment using VAS. J. Climate Appl. Meteor., 22, 377-384.
- Moore, T.J., R.L. Gall, and T.C. Adang, 1989: Disturbances along the Arizona summer monsoon boundary. Accepted for publication by Mon. Wea. Rev.
- Mosher, F.R., 1978: Cloud drift winds from geostationary satellites. Atmos. Tech., 10, 53-60.
- Petterssen, S., 1956: Weather Analysis and Forecasting, Volume II. McGraw-Hill, 266 pp.

## LIST OF REFERENCES--Continued

- Reap, R.M., 1986: Evaluation of cloud-to-ground lightning data from the western United States for the 1983-1984 summer seasons. J. Climate Appl. Meteor., 25, 785-799.
- Reitan, C.H., 1957: The role of precipitable water in Arizona's summer rains. Technical Reports on the Meteorology and Climatology of Arid Regions, No. 2, Institute of Atmospheric Physics, University of Arizona.
- Shapiro, M.A., 1981: Frontogenesis and geostrophically forced secondary circulations in the vicinity of jet stream-frontal zone systems. J. Atmos. Sci., 38, 954-973.
- Stewart, T.R., C.M. Hayden, and W.L. Smith, 1985: A note on water vapor wind tracking using VAS data on McIDAS. Bull. Amer. Meteor. Soc., 66, 1111-1115.
- Suomi, V.E., R. Fox, S.S. Limaye, and W.L. Smith, 1983: McIDAS III: A modern interactive data access and analysis system. J. Climate Appl. Meteor., 22, 765-778.
- Tang, M. and E.R. Reiter, 1984: Plateau Monsoons of the Northern Hemisphere: A Comparison between North America and Tibet. Mon. Wea. Rev., 112, 617-637.
- Wash, C.H. and T.M. Whittaker, 1980: Subsynoptic analysis and forecasting with an interactive computer system. Bull. Amer. Meteor. Soc., 61, 1584-1591.
- Wilson, T.A. and D.D. Houghton, 1979: Mesoscale wind fields for a severe storm situation determined from SMS cloud observations. Mon. Wea. Rev., 107, 1198-1209.